February 2022

PhD Dissertation

AI-Applied UWB Positioning System with Mitigated NLOS Effects

Graduate School of Chosun University

Department of Information and Communication Engineering

Dae-Ho Kim

AI-Applied UWB Positioning System with Mitigated NLOS Effects

NLOS 효과가 완화된
AI 적용 UWB 측위 시스템

February 25, 2022

Graduate School of Chosun University

Department of Information and Communication Engineering

Dae-Ho Kim

AI-Applied UWB Positioning System with Mitigated NLOS Effects

Advisor: Prof. Jae-Young Pyun

This thesis is submitted to the Graduate School of Chosun University in partial fulfillment of the requirements for the Doctor's degree in engineering.

October 2021

Graduate School of Chosun University

Department of Information and Communication Engineering

Dae-Ho Kim

This is to certify that the Doctor's thesis of

Dae-Ho Kim

has been approved by the examining committee for the thesis requirement for the Doctor's degree in engineering.

Committee Chairperson
Chosun University **Prof. Suk-Seung Hwang** (Sign)

Committee Member
Chosun University **Prof. Goo-Rak Kwon** (Sign)

Committee Member
Chonnam National University **Prof. KyungBaek Kim** (Sign)

Committee Member
Duksung Women's University **Prof. Tai-Won Um** (Sign)

Committee Member
Chosun University **Prof. Jae-Young Pyun** (Sign)

January 2022

Graduate School of Chosun University

Table of contents

List of tables

List of figures

Abstract

AI-Applied UWB Positioning System with Mitigated NLOS Effects

Dae-Ho Kim
Advisor : Prof. Jae-Young Pyun, Ph.D.
Dept. Info. and Comm. Eng.,
Graduate School of Chosun University

The ultra-wideband-based (UWB) indoor positioning system (IPS) has high positioning precision and accuracy and can meet the requirements of location-based services (LBSs) for Internet of Things (IoT) applications. However, there are usually a limited number of line-of-sight (LOS) channels in indoor environments. This thesis introduces the artificial intelligence (AI) applied UWB positioning system that can enhance the positioning performance of an IPS in a common indoor environment by classifying channel conditions based on ranging errors using the long short-term memory (LSTM) based deep learning (DL) model. The proposed system mitigates the positioning degradation caused by the NLOS effects by performing extended Kalman filter (EKF) localization based on the detected channel conditions. This study provides a detailed experimental setup and rigorous performance evaluation of the proposed system. The AI model is trained by the dataset collected from the testbed. Then, the testbed of the proposed positioning system is evaluated by conducting experiments consisting of a known scenario and

an unknown scenario. The evaluation results showed that the AI-EKF localization method of the proposed system significantly improved the positioning performance compared with the three existing positioning methods.

요 약

NLOS 효과가 완화된
AI 적용 UWB 측위 시스템

김 대 호

지도교수: 변 재 영

조선대학교 대학원 정보통신공학과

초광대역(UWB) 기반의 실내 측위 시스템은 사물 인터넷 응용기술로서 위치 기반 서비스의 요구 사항을 충족할 수 있는 높은 측위 정밀도와 정확도를 갖고 있다. 그러나, 일반적으로 실내 환경에서 UWB 기기간의 깨끗한 가시선 채널 조건을 찾는 것은 어렵다. 본 논문에서는 장단기 기억 셀(LSTM) 신경망 기반 심층 학습을 이용하여 UWB 거리 측정의 오차를 기반으로 채널 조건을 분류하고, 일반적인 실내 환경에서 측위 성능을 향상하기 위한 인공지능이 적용된 UWB 측위 시스템을 제안한다. 그리고, 감지된 채널 조건을 통해 확장 칼만 필터 측위 알고리즘을 수행하여 비 가시선 효과로 인한 측위 성능 저하를 완화한다. 또한, 이 논문은 제안된 시스템에 대해 상세한 실험 설정과 엄격한 성능 평가를 제공한다. 실험과 성능 평가를 위한 테스트베드 장치로부터 수집된 데이터 세트를 이용하여 LSTM 기반의 인공지능 모델을 훈련한 후, 인공지능 모델이 아는 시나리오와 알지 못한 시나리오로 구성된 실험에서 제안한 인공지능이 적용된 UWB 측위 시스템을 평가하였다. 평가 결과, 제안한 시스템의 인공지능이 적용된 확장 칼만 필터 측위 방법은 기존 3가지 측위 방식과 비교해 그 성

능이 크게 향상되는 것으로 나타났다.

I. Introduction

A. Research Background

Internet of Things (IoT) technologies have been incorporated in various ways in location-based applications depending on their applicability [1]. Specifically, ultra-wideband-based (UWB) indoor positioning systems (IPS) provide various indoor location-based services (LBSs), such as augmented reality (AR) [2], indoor unmanned aerial vehicles (UAV) [3], sports [4], automated guided vehicle (AVG) [5], and industrial tracking [6], requiring precise and stable positioning performance.

The UWB positioning system specified in [7][8] meets these requirements with its unique high-resolution timestamping, i.e., impulse radio (IR) signals emitted by UWB devices have nanoscale time resolution [9][10]. The time of arrival (TOA) or time difference of arrival (TDOA) between devices can be obtained from timestamps captured during the time of sending and receiving messages [11]. Then, the target position can be estimated using TOA or TDOA [12]. System designs based on TOA are more simple and common than TDOA-based positioning systems [13]; this provides flexibility for infrastructure construction. In addition, the TOA method primarily uses a two-way message exchange called two-way ranging (TWR). Therefore, it can estimate the distance without a time synchronization process by using round trip times between the tag and anchor [14][15]. Moreover, an enhanced message exchange method, such as double-sided-TWR (DS-TWR), can achieve cm-level distance measurement performance [16][17].

Distances measured with TWR are used in positioning systems using trilateration [18]. The tag position in trilateration is estimated using the intersection of the circles created by the distance between the tag and anchors. The least-squares (LS) method is used to derive the tag position from equation [15]. Furthermore, weighted LS (WLS) can be useful for improving the positioning performance by utilizing distance [19], residual variance [20], and estimated error [21] as the weight factor. A more advanced method involves applying a Kalman filter (KF) to position measurement [22]. In particular, extended KF (EKF) with linear approximation using the Taylor series is a well-known algorithm for linearizing and optimizing positioning systems with nonlinear designs such as tracking and navigation [20]. In practice, EKF has been used in various positioning systems such as autopilot of unmanned aerial vehicle (UAV) [23], inertial navigation [24], vehicle navigation [25], vehicle tracking using radar [26], etc. However, although the positioning algorithm has been advanced from the LS method to EKF localization, the UWB signals propagated in a complex indoor environment deteriorate the distance measurement performance owing to multipath. In other words, the channel condition between the tag and anchor is the most important factor for UWB positioning systems that rely on distance measurement between them.

Recently, more practical techniques for optimizing the UWB system by identifying the NLOS channel have been proposed [27]-[30]. These techniques estimate channel conditions by using radio parameters calculated from the channel impulse response (CIR) [31]. These radio parameters in NLOS identification methods are combined with machine learning (ML), such as support vector machine (SVM) [32][33], decision tree [34], random forest [35], expectation maximization

(EM) for Gaussian mixture model (GMM) [36], and multi-layer perceptron [37]. Recently, deep learning (DL) approaches have been considered owing to advances in hardware for parallel computing. DL extracts features by itself during the learning process. DL-based methods such as convolutional neural networks (CNNs) and long short-term memory (LSTM) use the raw CIR sequence directly instead of the radio parameters calculated from the UWB device to enhance the accuracy of the channel classification [21], [38]-[41]. Artificial intelligence (AI) approaches for ML and DL have achieved LOS/NLOS classification accuracy of above 80 %.

B. Research Objective

This thesis introduces the AI-applied UWB positioning system that classifies channel conditions into 10-levels based on a ranging error distribution and mitigates the NLOS-induced error of TWR with the proposed AI-EKF localization.

C. Thesis Organization

The remainder of this thesis is organized as follows. In Section II, the relevant techniques for the proposed UWB system are described. Section III presents the proposed UWB positioning system and its AI-EKF localization method. Sections IV and V provide the experimental setup for performance evaluation and results. Finally, Section VI concludes the paper.

II. Background

A. NLOS Effects of UWB Ranging

1) Error Model of UWB Ranging

When the first signal arrives at the UWB receiver, UWB signals propagated at the channel are captured, and their timestamps are recorded for the distance measurement. In a clean LOS channel, the first arrived signal is assumed to be the signal that traversed the shortest path, i.e., the ranging result obtained from TWR is close to the actual distance between the tag and anchor. On the other hand, in the NLOS channel, the first path signal is generated by multipath interference and obstacle penetration waves [42]-[44]. In this situation, UWB timestamps vary and can be presented with a positive bias in the multipath propagation environment [12] [45][46]. Therefore, the UWB ranging performance based on timestamps is affected by the channel conditions. In this paper, the ranging result d is assumed as follows:

$$d = \begin{cases} d_{act} + e_{meas} & \text{for LOS channel} \\ d_{act} + e_{meas} + b_{nlos} & \text{for NLOS channel'} \end{cases} \quad (1)$$

where d_{act} is the actual distance between the tag and anchor, $e_{meas} \sim N(0, \sigma_m^2)$ denotes the measurement error defined as additive white Gaussian noise (AWGN) with zero mean and variance σ_m^2, and b_{nlos} represents a positive NLOS-biased error defined as an exponential random variable [47]-[49].

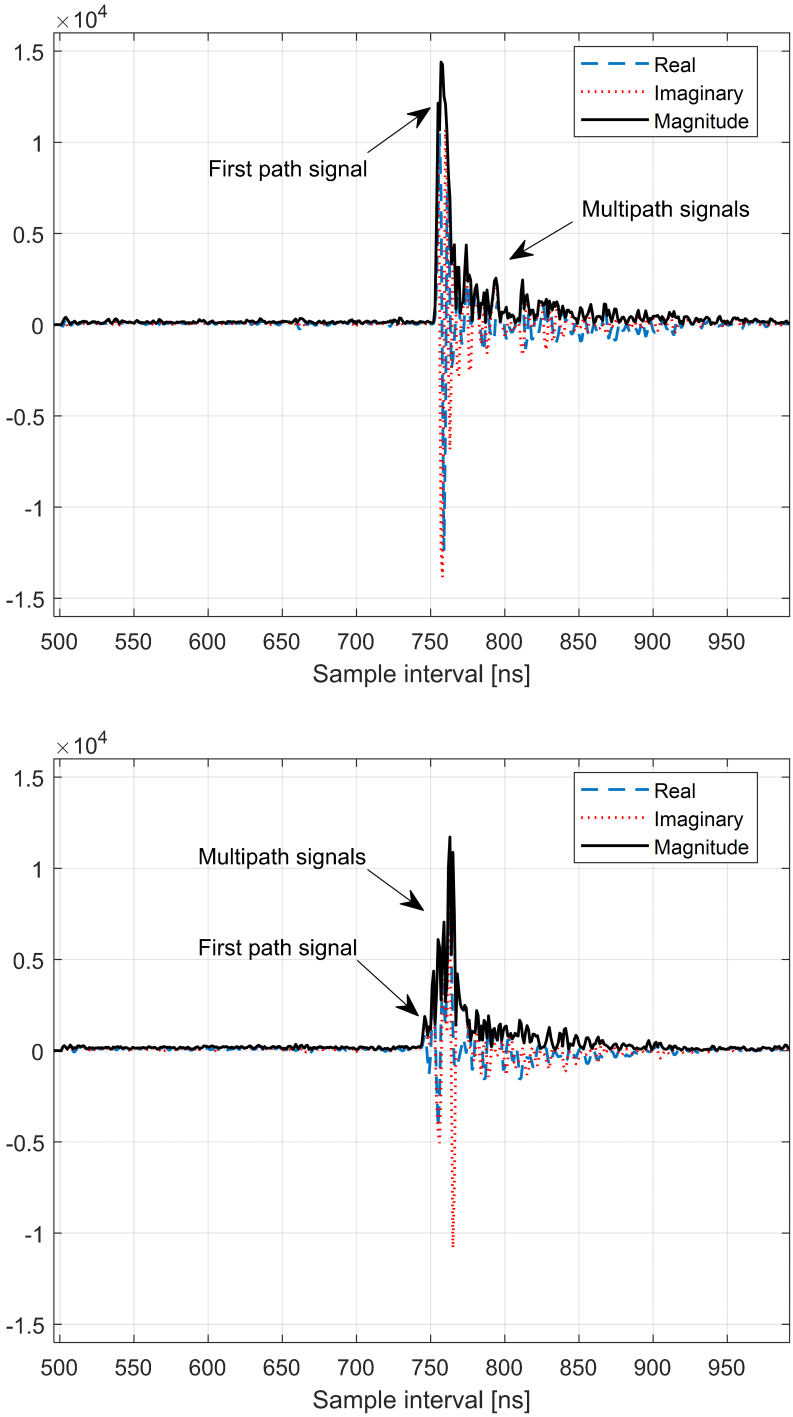

Figure 1. Received UWB signals indicated as CIR: (top) LOS channel (bottom) NLOS channel.

The deciding factor for the channel condition is required to approximate the error parameters of e_{meas} and b_{nlos}. Fig. 1 shows the real and imaginary components of the received UWB signals in LOS and NLOS channels indicated as CIR [50]. In this figure, the first path signal measurements of both LOS and NLOS channels are shown. In the LOS channel, CIR had a strongly concentrated energy distribution at the arrival time of the first path signal, which was observed at a sampling time of 750 ns. In contrast, in the NLOS channel, the overall power of the UWB signal was weakened by obstacle penetration and multipath interference and was observed at a sampling time of 747 ns. In this example, the signal measured at 758 ns was stronger than the first path signal; this UWB signal interfered constructively and destructively in a cluttered environment.

2) Classification of Channel Conditions

In this thesis, DL was used on the CIR to determine the channel condition. The recurrent neural network (RNN) model was selected because CIR is a time-series data-type. RNN adopts a recurrent operation, such that the output (hidden state) generated from the previous time step is provided in the current time step. This recurrent operation process enables the optimal display of the time-series data pattern. In addition, RNN can be designed with different dimension sizes at the input and output. In this research, the many-to-one model, an RNN input/output model, is considered for classifying channel conditions using a sequence of inputs. However, a simple RNN has a long-term dependency problem, as past information cannot propagate sufficiently to the current one owing to a gradient vanishing in the backpropagation process [51]-[53].

The LSTM network was proposed in [54] to avoid the long-term dependency problem [55] of a simple RNN. It improves the inference and learning performance of a complex sequence by recalling the past state. Fig. 2 illustrates the LSTM cell and its components, where f, i, o, and g represent the forget gate, input gate, output gate, and cell candidate, respectively. The formula for the components at time step t is expressed as:

$$\begin{cases} f_t = sigmoid(W_I^f X_t + W_R^f h_{t-1} + b_f) \\ i_t = sigmoid(W_I^i X_t + W_R^i h_{t-1} + b_i) \\ o_t = sigmoid(W_I^o X_t + W_R^o h_{t-1} + b_o) \\ g_t = \tanh(W_I^g X_t + W_R^g h_{t-1} + b_g) \\ c_t = f_t \bullet c_{t-1} + i_t \odot g_t \\ h_t = o_t \odot \tanh(c_t) \end{cases}, \tag{2}$$

where c_t and h_t denote the cell and hidden states, respectively. In addition, W_I, W_R, and b represent the input weight, recurrent weight, and bias, respectively. X_t is the input sequence, which is represented as CIR.

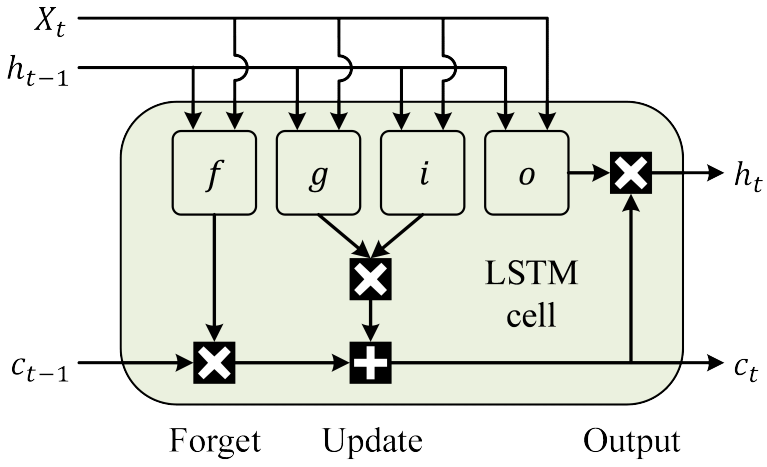

Figure 2. Components of the LSTM cell.

B. Ranging Protocols

The TWR is a message-exchange procedure for estimating the distance between UWB radios. It has the advantage of observing the distance on both tag and anchor sides owing to the message exchange of the TWR. Therefore, the position of the tag can be observed at either tag or anchor side (connected to a server) by employing trilateration with the estimated distances between the tag and the surrounding anchors. Furthermore, when the tag calculated its position, anchors could be configured as lightweight devices without additional communication infrastructure such as ethernet and WiFi to connect with the positioning server [56]. In this work, the proposed UWB positioning system adopts TWR because of its flexible operating conditions.

1) Two-Way Ranging (TWR)

Fig. 3 presents the TWR introduced in IEEE 802.15.4-2011 std. [7] and IEEE 802.15.8 std. [8]. In this figure, a tag device and an anchor are illustrated as Tag and Anchor boxes, respectively. First, the tag sends a ranging request message to the anchor and stores TS_1 at the tag device as a TX timestamp. The anchor receives a request message from the tag and stores TS_2 as an RX timestamp. Next, the anchor sends a response message to the tag after a reply time (T_{reply}) and stores TS_3 at the anchor device as a TX timestamp. Finally, the tag stores TS_4 after obtaining the response message as an RX timestamp. In this message-exchange procedure, timestamps are obtained by capturing the ranging marker designated in the UWB system. The ranging marker specified in [7] is

located at the start of the first symbol of the physical layer (PHY) header of the frame.

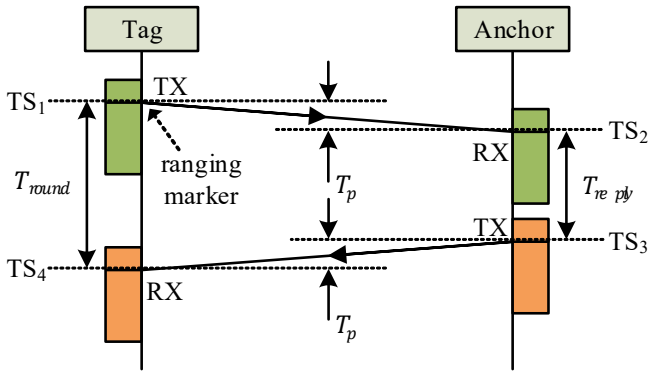

Figure 3. Two-way ranging (TWR).

After the message-exchange is complete, the round trip time (T_{round}) and T_{reply} of the ranging messages are measured using stored timestamps TS_1, TS_2, TS_3, and TS_4 observed in the tag and anchor as follows:

$$T_{round} = TS_4 - TS_1, \tag{3}$$

$$T_{reply} = TS_3 - TS_2, \tag{4}$$

Then, the propagation time T_p, that is, TOA of the UWB ranging message, can be estimated as follows:

$$T_p = \frac{T_{round} - T_{reply}}{2}, \tag{5}$$

Therefore, the distance d between the tag and anchor is:

$$d = T_p \times c, \tag{6}$$

where c is the speed of light (299,792,458 m/s).

As shown in Fig. 3, the TWR based TOA estimation does not demand time synchronization between tag and anchor because T_{round} and T_{reply} are observed independently at each device. This advantage makes it easier to build positioning systems. However, a single-sided TWR has a weakness in that the TOA estimation error can be increased by the longer TWR message processing time (T_{reply}) because of the hardware clock skew between the tag and anchor [57]. Thus, the double-sided TWR (DS-TWR) was devised to solve the clock skew problem by measuring the TOA at each side of the tag and anchor.

2) Double-Sided TWR (DS-TWR)

The DS-TWR procedure is illustrated in Fig. 4.

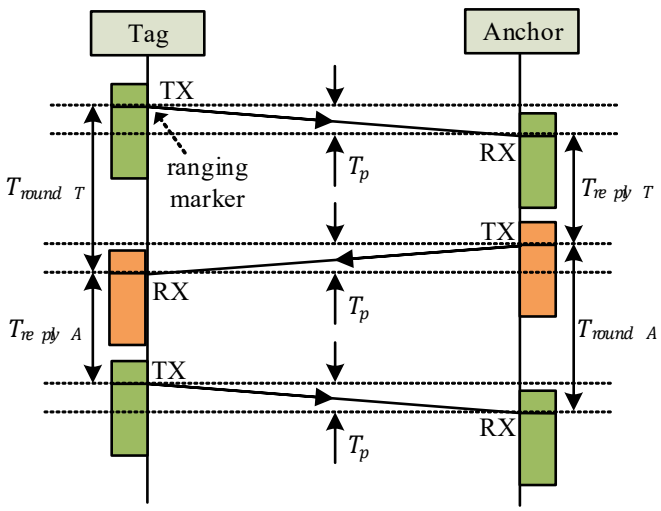

Figure 4. Double-sided TWR (DS-TWR).

In DS-TWR, the tag and anchor initiate a TWR message exchange, which is the same as typical TWR obtaining TOA on the tag side. After obtaining the first TOA, the tag sends a second ranging message to the anchor for the second TOA. Finally, the response of the anchor and second ranging messages of the tag are used to obtain the second TOA on the anchor-side during this process. Thus, T_p of the DS-TWR is measured by

$$T_p = \frac{T_{roundT} \times T_{roundA} - T_{replyT} \times T_{replyA}}{T_{roundT} + T_{roundA} + T_{replyT} + T_{replyA}}. \quad (7)$$

3) DS-TWR with Multiple Acknowledgment (DS-TWR-MA)

In general, the TWR-based UWB positioning system inevitably requires three or more anchors for the estimation of the tag location. Indeed, to provide the navigation services based on DS-TWR, each tag needs at least nine transfers because DS-TWR performs three message exchanges with three anchors. This operation requires a large on-air time and battery power to obtain the position of each tag. One of the commercial UWB manufacturers, Decawave, introduced a practical DS-TWR, DS-TWR with multiple acknowledgment (DS-TWR-MA), for its real-time location system (RTLS) service [50], which improved the power consumption and on-air time in TWR message exchanges. It is based on the symmetric DS-TWR with multiple acknowledgment (SDS-TWR-MA) [58].

Fig. 5 shows the distance measurement operation of the DS-TWR-MA procedure. In this example, the tag initiates the broadcasting of a poll message to anchors (A0

~ A2). The anchors receiving a poll message from the tag then send response messages sequentially after a predefined reply time ($T_{replyT0}$, $T_{replyT1}$, and $T_{replyT2}$). Next, the tag receiving response messages from the anchors sends a final message to the anchors. Finally, the anchor receiving the final message completes the ranging message exchange. As a result, the propagation time T_{pN} for anchor number n is calculated by the stored timestamps as follows:

$$T_{pn} = \frac{T_{roundTn} \times T_{roundAn} - T_{replyTn} \times T_{replyAn}}{T_{roundTn} + T_{roundAn} + T_{replyTn} + T_{replyAn}}, \tag{8}$$

where n is 0, 1, and 2 in the example shown in Fig. 5.

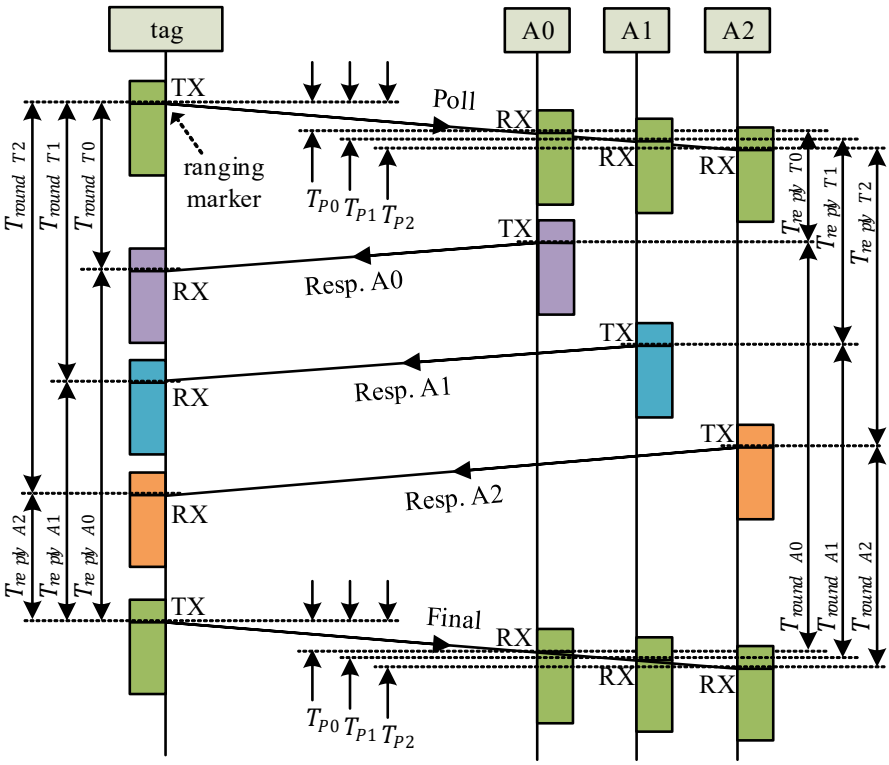

Figure 5. DS-TWR with multiple acknowledgment (DS-TWR-MA).

C. Localization Methods for UWB Positioning

1) Trilateration with Least-Square Solution

Trilateration is the process of determining an unknown position with a mathematical calculation for estimating the relative position by applying a geometry of circles and spheres. Fig. 6 shows anchors A0 ~ A2 located in their known positions $(x_0,\ y_0)$ ~ $(x_2,\ y_2)$, whereas the distances d_0 ~ d_2 between a tag and anchors are obtained using the TWR.

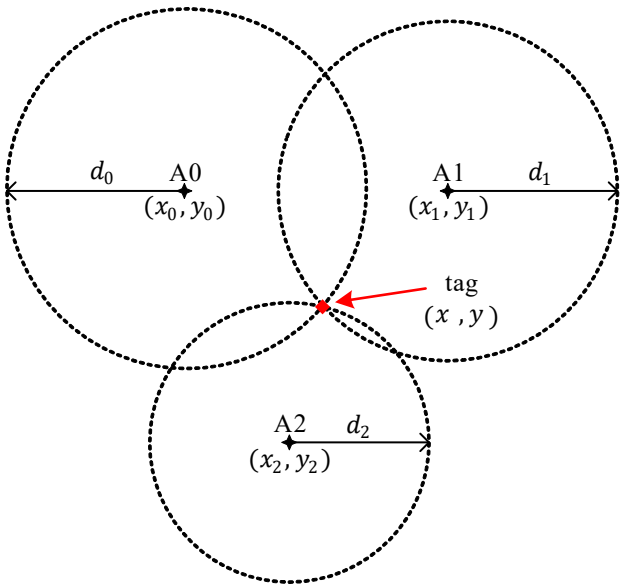

Figure 6. TWR-based UWB positioning in 2D (trilateration).

Fig. 6 shows TWR-based positioning in two-dimensional space; the tag position becomes the intersection of the created circles and is expressed by the formula as follows:

$$\begin{cases} (x_0 - x)^2 + (y_0 - y)^2 = d_0^2 \\ (x_1 - x)^2 + (y_1 - y)^2 = d_1^2 \\ (x_2 - x)^2 + (y_2 - y)^2 = d_2^2 \\ \vdots \\ (x_n - x)^2 + (y_n - y)^2 = d_n^2 \end{cases}, \tag{9}$$

where d_n is the distance between the tag located at $(x,\ y)$ coordinates and the pre-deployed nth anchor located at $(x_n,\ y_n)$ coordinates.

In practical applications, the LS method can be used for the approximation of the tag position because ranging errors do not create a single intersection [15]. The LS solution for the tag position $(x,\ y)$ is listed as follows:
Firstly, (9) is expanded to get

$$\begin{cases} -2x_0x - 2y_0y + x^2 + y^2 = d_0^2 - x_0^2 - y_0^2 \\ -2x_1x - 2y_1y + x^2 + y^2 = d_1^2 - x_1^2 - y_1^2 \\ -2x_2x - 2y_2y + x^2 + y^2 = d_2^2 - x_2^2 - y_2^2 \\ \vdots \\ -2x_nx - 2y_ny + x^2 + y^2 = d_n^2 - x_n^2 - y_n^2 \end{cases}, \tag{10}$$

then applied secondly with $\boldsymbol{\Gamma\epsilon = \beta}$ form

$$\boldsymbol{\Gamma} = \begin{bmatrix} -2x_0 & -2y_0 & 1 \\ -2x_1 & -2y_1 & 1 \\ -2x_2 & -2y_2 & 1 \\ \vdots & \vdots & \vdots \\ -2x_n & -2y_n & 1 \end{bmatrix}, \tag{11}$$

$$\boldsymbol{\epsilon} = \begin{bmatrix} x \\ y \\ x^2 + y^2 \end{bmatrix}, \tag{12}$$

$$\boldsymbol{\beta}=\begin{bmatrix} d_0^2-x_0^2-y_0^2 \\ d_1^2-x_1^2-y_1^2 \\ d_2^2-x_2^2-y_2^2 \\ \vdots \\ d_n^2-x_n^2-y_n^2 \end{bmatrix}. \tag{13}$$

Now, a vector $\boldsymbol{\epsilon}$ for tag location can be approximated as

$$\boldsymbol{\epsilon}=(\boldsymbol{\Gamma}^T\boldsymbol{\Gamma})^{-1}\boldsymbol{\Gamma}^T\boldsymbol{\beta}. \tag{14}$$

TWR tends to increase errors due to clock skew and multipath as the distance between the devices increases. Hence, the LS solution has a limitation in multipath environments because it uses the same weight for the distance measurement of each anchor. WLS can improve the positioning performance by applying a weight factor for the distance measurement [20][21]. The distance-weighted WLS solution $\boldsymbol{\chi}$ and its weight matrix $\boldsymbol{\Theta}$ are expressed as follows:

$$\boldsymbol{\chi}=(\boldsymbol{\Gamma}^T\boldsymbol{\Theta}\boldsymbol{\Gamma})^{-1}\boldsymbol{\Gamma}^T\boldsymbol{\Theta}\boldsymbol{\beta}, \tag{15}$$

$$\boldsymbol{\Theta}=\begin{bmatrix} \frac{1}{d_0} & 0 & \cdots & 0 \\ 0 & \frac{1}{d_1} & \cdots & 0 \\ \vdots & \vdots & \ddots & 0 \\ 0 & 0 & 0 & \frac{1}{d_n} \end{bmatrix}. \tag{16}$$

WLS can enhance the estimation performance of the tag location but is not adaptive to unstable measurement noise.

2) Extended-Kalman Filter (EKF) Localization

In this thesis, the proposed UWB system includes the EKF localization introduced in [20][22]. It was assumed that the target pedestrian moves the tag in a straight path with uniform velocity and acceleration in the 2D plane. Hence, a state vector $\mathbf{X}_k$ at the time step k is expressed as follows:

$$\mathbf{X}_k = \begin{bmatrix} x_k \\ y_k \\ v_k^x \\ v_k^y \\ a_k^x \\ a_k^y \end{bmatrix} = \begin{bmatrix} x_{k-1} + v_{k-1}^x T_s + \frac{1}{2} a_{k-1}^x T_s^2 + \frac{T_s^3}{6} w_{k-1}^x \\ y_{k-1} + v_{k-1}^y T_s + \frac{1}{2} a_{k-1}^y T_s^2 + \frac{T_s^3}{6} w_{k-1}^y \\ v_{k-1}^x + a_{k-1}^x T_s + \frac{T_s^2}{2} w_{k-1}^x \\ v_{k-1}^y + a_{k-1}^y T_s + \frac{T_s^2}{2} w_{k-1}^y \\ a_{k-1}^x + T_s w_{k-1}^x \\ a_{k-1}^y + T_s w_{k-1}^y \end{bmatrix}, \tag{17}$$

where x_k and y_k are the coordinates of the tag, v_k^x and v_k^y are the velocities, and a_k^x and a_k^y are the accelerations. Hence, the state equation of UWB localization is expressed as

$$\mathbf{X}_k = \mathbf{A}\mathbf{X}_{k-1} + \mathbf{G}\mathbf{W}_{k-1}, \tag{18}$$

where $\mathbf{W}_{k-1} = \begin{bmatrix} w_{k-1}^x w_{k-1}^y \end{bmatrix}$ is the process noise vector expressed as the covariance matrix $\mathbf{Q}_{k-1} = diag(\sigma_{a^x}^2, \sigma_{a^y}^2)$ and zero mean, and $\mathbf{A}$ and $\mathbf{G}$ expressed in (19) and (20) denote the state transition matrix and the noise driving matrix, respectively.

$$\mathbf{A}=\begin{bmatrix} 1 & 0 & T_s & 0 & \frac{T_s^2}{2} & 0 \\ 0 & 1 & 0 & T_s & 0 & \frac{T_s^2}{2} \\ 0 & 0 & 1 & 0 & T_s & 0 \\ 0 & 0 & 0 & 1 & 0 & T_s \\ 0 & 0 & 0 & 0 & 1 & 0 \\ 0 & 0 & 0 & 0 & 0 & 1 \end{bmatrix}, \tag{19}$$

$$\mathbf{G}=\begin{bmatrix} \frac{T_s^3}{6} & 0 \\ 0 & \frac{T_s^3}{6} \\ \frac{T_s^2}{2} & 0 \\ 0 & \frac{T_s^2}{2} \\ T_s & 0 \\ 0 & T_s \end{bmatrix}, \tag{20}$$

where T_s is the sample time.

Let $\mathbf{Z}_k$ denote the measurement vector for each TWR between the tag and anchor n, including the actual distance d_{nk} with the measurement noise v_{nk} at the time step k. Hence, the measurement equation of UWB ranging is expressed as follows:

$$\mathbf{Z}_k=\begin{bmatrix} d_{0k}+v_{0k} \\ d_{1k}+v_{1k} \\ d_{2k}+v_{2k} \\ \vdots \\ d_{nk}+v_{nk} \end{bmatrix}=\mathrm{m}(\mathbf{X}_k)+\mathbf{v}_k, \tag{21}$$

$$\mathrm{m}(\mathbf{X}_k) = \begin{bmatrix} \sqrt{(x_k - x_0)^2 + (y_k - y_0)^2} \\ \sqrt{(x_k - x_1)^2 + (y_k - y_1)^2} \\ \sqrt{(x_k - x_2)^2 + (y_k - y_2)^2} \\ \vdots \\ \sqrt{(x_k - x_n)^2 + (y_k - y_n)^2} \end{bmatrix}, \tag{22}$$

where $\mathbf{v}_k$ represents the measurement noise vector denoted as the covariance matrix $\mathbf{R}_k = diag(\sigma_{d_0}^2, \sigma_{d_1}^2, \cdots, \sigma_{d_n}^2)$, and zero mean. Because (22) is a nonlinear function, the Jacobian matrix of (22), $\mathbf{H}_k$ is required as follows:

$$\mathbf{H}_k = \begin{bmatrix} \frac{\partial d_{0k}}{\partial x_k} & \frac{\partial d_{0k}}{\partial y_k} & 0 & 0 & 0 & 0 \\ \frac{\partial d_{1k}}{\partial x_k} & \frac{\partial d_{1k}}{\partial y_k} & 0 & 0 & 0 & 0 \\ \frac{\partial d_{2k}}{\partial x_k} & \frac{\partial d_{2k}}{\partial y_k} & 0 & 0 & 0 & 0 \\ \vdots & \vdots & \vdots & \vdots & \vdots & \vdots \\ \frac{\partial d_{nk}}{\partial x_k} & \frac{\partial d_{nk}}{\partial y_k} & 0 & 0 & 0 & 0 \end{bmatrix}, \tag{23}$$

where

$$\begin{cases} \dfrac{\partial d_{nk}}{\partial x_k} = \dfrac{x_k - x_n}{\sqrt{(x_k - x_n)^2 + (y_k - y_n)^2}} \\ \dfrac{\partial d_{nk}}{\partial y_k} = \dfrac{y_k - y_n}{\sqrt{(x_k - x_n)^2 + (y_k - y_n)^2}} \end{cases}. \tag{24}$$

The procedure for EKF localization algorithm in the 2D plane is shown in Fig. 7. The prediction and correction phases were performed at time step k with positioning interval time T_s.

Algorithm 1: EKF localization for UWB system

Input: $\mathbf{Z}_k$
Output: $\hat{\mathbf{X}}_k$
Initialize: Initial state $\hat{\mathbf{X}}_0 = \chi_0$, error covariance matrix $\mathbf{P}_0 = var[\hat{\mathbf{X}}_0]$
for k=0:∞ **do**
  // EKF time update
  Phase `Prediction`$(\hat{\mathbf{X}}_{k-1}, \mathbf{P}_{k-1})$**:**
    // Predict the state ahead
    $\hat{\mathbf{X}}_k^- = \mathbf{A}\hat{\mathbf{X}}_{k-1}$
    // Predict the error covariance ahead
    $\mathbf{P}_k^- = \mathbf{A}\mathbf{P}_{k-1}\mathbf{A}^T + \mathbf{G}\mathbf{Q}_{k-1}\mathbf{G}^T$
    // Return a priori estimates
    return $\hat{\mathbf{X}}_k^-, \mathbf{P}_k^-$

  // EKF measurement update
  Phase `Correction`$(\hat{\mathbf{X}}_k^-, \mathbf{P}_k^-, \mathbf{Z}_k)$**:**
    // Compute the Kalman gain
    $\mathbf{K}_k = \mathbf{P}_k^- {\mathbf{H}_k}^T (\mathbf{H}_k \mathbf{P}_k^- {\mathbf{H}_k}^T + \mathbf{R}_k)^{-1}$
    // Correct estimate with measurement
    $\hat{\mathbf{X}}_k = \hat{\mathbf{X}}_k^- + \mathbf{K}_k(\mathbf{Z}_k - \mathrm{m}(\hat{\mathbf{X}}_k^-))$
    // Correct the error covariance
    $\mathbf{P}_k = \mathbf{P}_k^- - \mathbf{K}_k\mathbf{H}_k\mathbf{P}_k^-$
    // Return a posteriori estimates
    return $\hat{\mathbf{X}}_k, \mathbf{P}_k$

Figure 7. Algorithm of EKF localization for UWB positioning system.

III. AI-Applied UWB Positioning System

The EKF can be used to estimate the UWB tag in an LOS environment. However, in an NLOS environment with dynamic indoor conditions, the location estimation performance is degraded owing to the variation in the measurement model, which is influenced by NLOS conditions. Therefore, a positioning method that identifies the NLOS channel conditions and updates the measurement model is required. In this study, a UWB positioning system is proposed to improve the NLOS identification of EKF localization. Fig. 8 illustrates the experimental environment of the proposed system comprising pre-deployed anchors, tag, and host computer. First, the UWB tag of this system performs DS-TWR+ with anchors to capture the distance and its CIR. Then, it transfers the anchor ID (number), distance, CIR stream, additional link diagnostic data, and its cyclic redundancy check (CRC) to the host computer, which estimates the tag position using AI-EKF localization. Depending on the application, the UWB tag and host computer can be integrated or separated from each other.

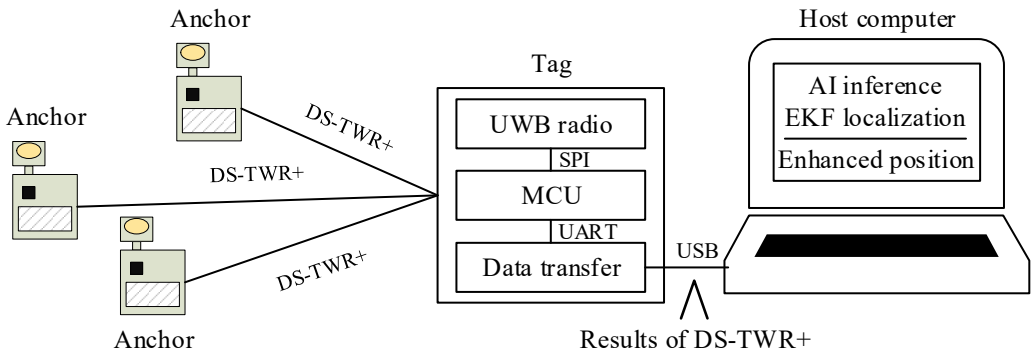

Figure 8. Experimental environment of the AI-applied UWB positioning system.

Fig. 9 presents a flowchart for the AI-EKF localization of the proposed UWB positioning system. First, DS-TWR+ obtains the distance and CIR between the tag and anchors. Then, the CIR is provided as input to the AI inference step, which includes a trained LSTM classification network for channel conditions. Next, the NLOS mitigation block reduces the NLOS error of the obtained distance using the channel condition determined at the AI inference step. Subsequently, it generates the NLOS mitigated measurement vector containing the distance and its noise parameter required for EKF localization, which is expressed as $\hat{\mathbf{Z}}_k$ and $\hat{\mathbf{R}}_k$. Finally, the EKF localization adopts the NLOS mitigated measurement at its correction phase and provides the current position. The remainder of this section comprehensively describes the AI inference and NLOS mitigation block.

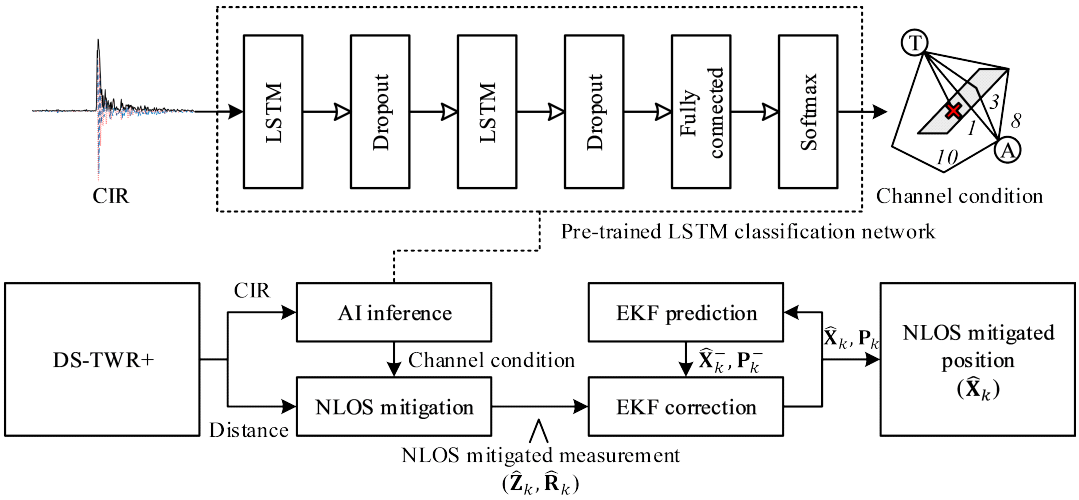

Figure 9. AI-EKF localization of the proposed positioning system.

A. DS-TWR with a Report Message (DS-TWR+)

In this study, the observed distance is reported to the tag via a message *Report* and is used to estimate the tag position. In addition, the message *Report* signal is employed to measure the CIR and determine the channel condition. Distance observation and CIR measurement are conducted after the TWR message exchange because these operations may interrupt the transmission times of TWR messages. Actually, the TWR approach is expected to operate during a limited short processing time owing to the clock skew problem. However, when CIR is measured and used for the channel classification, the tag consumes a relatively longer processing time because CIR is a data stream with a size of several Kbytes and is recorded to the memory of the UWB device.

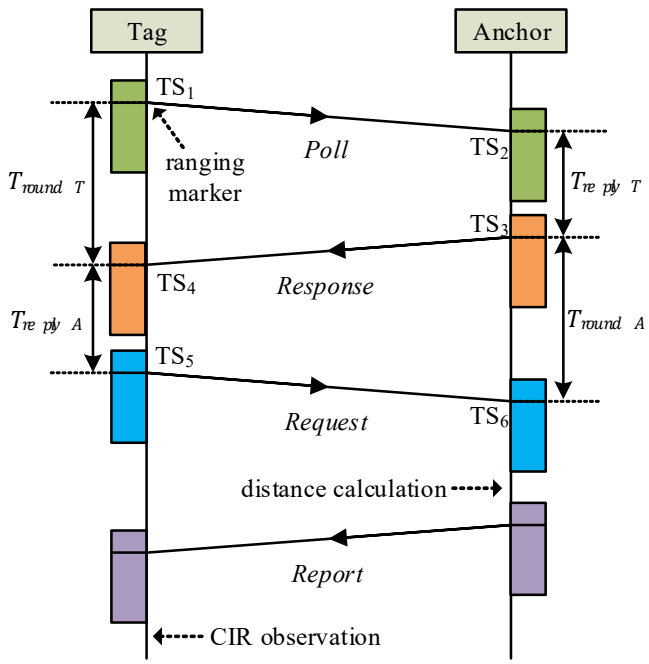

Figure 10. Double-sided TWR with report message (DS-TWR+).

The tag of the proposed system has to access the CIR stored at the memory and transfer it to the host computer without interrupting other process works. The processing time for the CIR management should be guaranteed for beneficial CIR-based positioning performance. Therefore, DS-TWR-MA is unsuitable for the proposed system because of its streamlined message-exchange procedure. Hence, a better TWR is introduced in this thesis. Fig. 10 presents a DS-TWR with a report message named DS-TWR+. As illustrated in this figure, the message exchange of the DS-TWR producing timestamps from TS_1 to TS_6 is adopted to DS-TWR+. The tag sends captured timestamps TS_1, TS_4, and TS_5 within the message *Request* to the anchor, as all timestamps are required for distance calculation. Subsequently, the anchor handles the received message *Request* and its stored timestamps TS_2, TS_3, and TS_6 to obtain T_{round} and T_{reply} of both tag and anchor sides as follows:

Tag side:

$$T_{roundT} = TS_4 - TS_1, \tag{25}$$

$$T_{replyT} = TS_3 - TS_2. \tag{26}$$

Anchor side:

$$T_{roundA} = TS_6 - TS_3, \tag{27}$$

$$T_{replyA} = TS_5 - TS_4. \tag{28}$$

Hence, these timing factors apply to (7).

The DS-TWR+ presented in Fig. 10 comprises four ranging messages. Among these messages, *Poll*, *Response*, and *Request* generate timestamps that are adopted for distance calculation. Message *Report* conveys the obtained distance from the

anchor to the tag and is itself used for the CIR observation. In this DS-TWR+, each message is also encoded based on the IEEE 802.15.4 std. [7] medium access control (MAC) data frame comprising a MAC header (MHR), MAC payload, and MAC footer (MFR), as illustrated in Fig. 11.

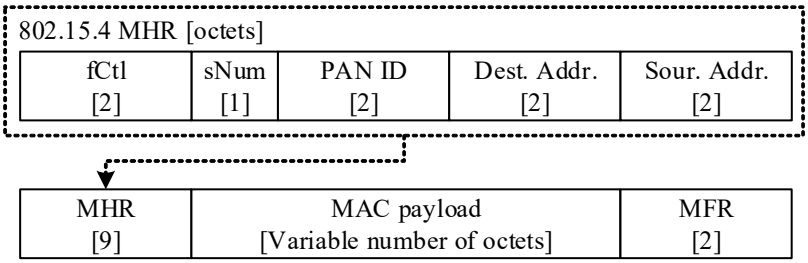

Figure 11. DS-TWR+ frame format.

Specifically, the MHR includes fields for the message identification as follows: frame control (fCtl), sequence number (sNum), destination PAN identifier (PAN ID), destination address, and source address. The fCtl of two-octets expresses the frame type, PAN ID compression, destination addressing mode, and source addressing mode as presented in Table 1. In this configuration, ranging messages of DS-TWR+ adopt the PAN ID compression and the short addressing mode, because DS-TWR+ has been designed to minimize its frame length for the fast ranging process.

Table 1. Frame control field of the MHR used in DS-TWR+.

Sub-field	Bits	Value	Description
Frame type	0 – 2	$001_{(2)}$	Data frame
PAN ID compression	6	$1_{(2)}$	Enabled
Destination addressing mode	10 – 11	$01_{(2)}$	Short address mode (16 bits)
Source addressing mode	14 – 15	$01_{(2)}$	Short address mode (16 bits)

The MAC payload with the variable number of octets contains the ranging

message type (mType) of a single octet and the attached data, such as timestamps and calculated distance. Table 2 presents the MAC payload defined for each ranging message, where the messages *Poll* and *Response* have no attached data and the message *Request* delivers timestamps TS_1, TS_4, and TS_5 to the anchor. In addition, message *Report* contains a calculated distance of four octets. In this ranging approach, the timestamp unit of approximately 15.65 ps and a single-precision floating-point format are employed for the distance estimation.

Table 2. MAC payload definition for each ranging message.

Message	mType	Attached data [octets]
Poll	$AA_{(16)}$	-
Response	$BB_{(16)}$	-
Request	$CC_{(16)}$	Timestamps of the tag [15]
Report	$DD_{(16)}$	Distance [4]

The MFR field of two-octets has the frame checking sequence (FCS) used for the cyclic redundancy check (CRC) conducting error detection on the transmitted frame. Fig. 12 presents the DS-TWR+ frame structure for each ranging message comprising the MHR of 9 octets, MAC payload of 1 – 16 octets, and FCS of 2 octets. As illustrated in Fig. 12 (a), messages *Poll* and *Response* have the same size of 12 octets. Furthermore, the message *Request* of Fig. 12 (b) containing timestamps uses a frame length of 27 octets, while the message *Report* of Fig. 12 (c) with a distance estimation result has 16 octets.

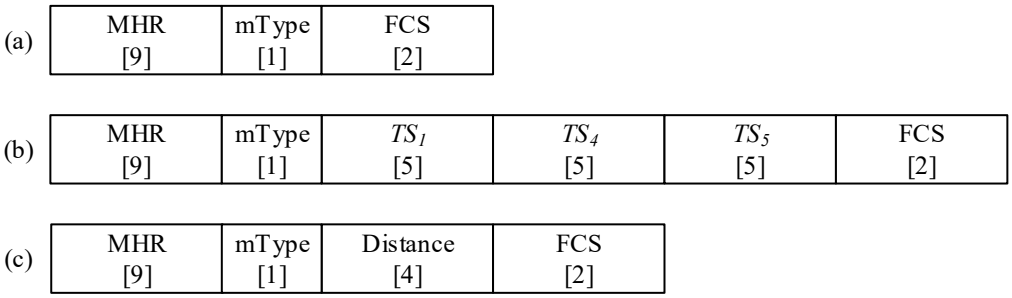

Figure 12. DS-TWR+ frames for each message: (a) *Poll* and *Response* (b) *Request* (c) *Report*.

In addition, Fig. 13 presents the packet format of the *Result* used for the delivery of the estimated distances to the host computer performing EKF localization to identify the tag location in our study. It comprises fCnt of 2 bytes, UWB-operating mode of a single byte, aID of a single byte, sNum of a single byte, calculated distance from *Report*, UWB RX diagnostic data of 16 bytes, CIR signal captured from *Report* of 1984 bytes, and FCS generated by 32-bit CRC.

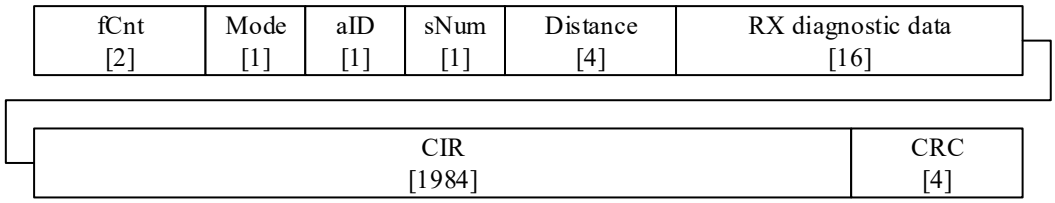

Figure 13. Packet format of *Result* transmitted from the tag.

In the *Result* format, fCnt is increased whenever the tag completes DS-TWR+ with each anchor. In addition, it is adopted as the time step (k) of EKF localization. Mode expresses the configuration of the UWB system such as channel, preamble length, etc. aID indicates an anchor identifier that represents a destination address of messages *Poll* and *Request*. sNum and distance represent the sequence

number and estimated distance obtained from MHR and MAC payload of message *Report*, respectively. The RX diagnostic data for message *Report* provides the status of received signals such as received signal power level (RSL), signal power in the first path (FSL), first path index of CIR, etc [59]. The CIR field presents the received UWB signal comprising real and imaginary parts of 2 bytes each, where the CIR length is 496, as illustrated in Fig. 1. CRC for data integrity has an output of CRC-32 [60] computed for the *Result* packet. Finally, the host computer performing localization confirms the CRC field and operates AI-EKF using the data obtained from the received *Result* packet.

The testbed devices, DS-TWR+ tag and anchors, are developed based on the Decawave driver API [59], TWR implementation guide [61], and Mbed OS [62]. The driver API controls the UWB transceiver that generates interrupt requests (IRQ) to receive and transmit frames. Furthermore, Mbed OS, a real-time operating system (RTOS), is adopted as the task scheduler for a finite-state machine (FSM) at DS-TWR+ devices.

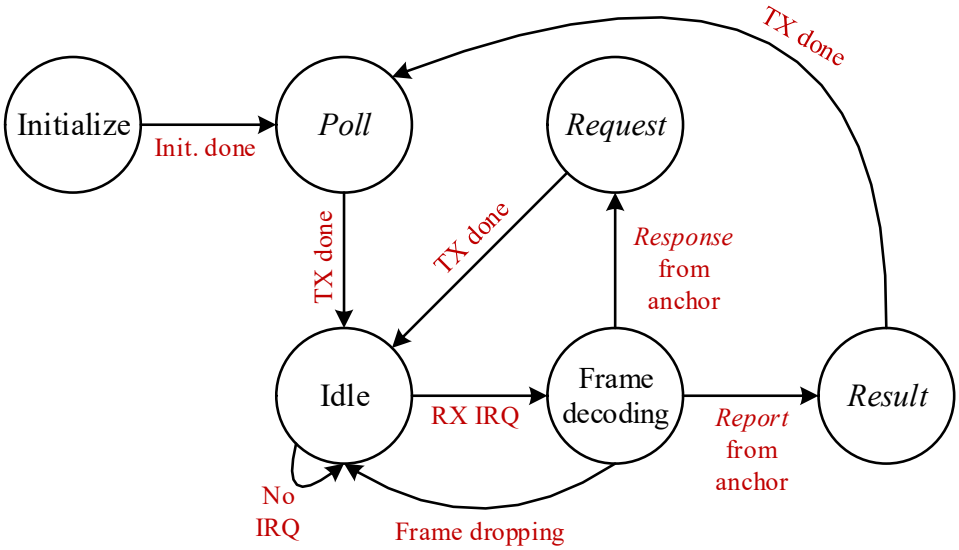

Figure 14. Tag operation of DS-TWR+ represented with FSM state diagram.

Fig. 14 presents the tag operation of DS-TWR+ with the FSM state diagram. First, the tag starts the DS-TWR+ operation by initializing its UWB PHY and MAC configurations. Then, it prepares for the frame of message *Poll* including a target anchor number as the destination address and transfers it to the UWB channel. Next, the state of the FSM shifts to Idle and waits for RX IRQ. Subsequently, the tag decodes the received frame when RX IRQ occurs. The MHR and mType of the received frame are interpreted at this state. When the received frame is the message *Response* as an acknowledgment to the message *Poll*, the *Request* state is invoked, which transmits message *Request* with recorded time stamps TS_1 and TS_4, and TS_5. Then, DS-TWR+ returns to the Idle state again. After obtaining RX IRQ for the message *Report* reception, the tag obtains the estimated distance from the received message *Report* and captures its CIR signal at the frame decoding state. Finally, the state becomes *Result*, which transfers the estimated distance and its CIR observation of DS-TWR+ to the host computer for the localization in this study.

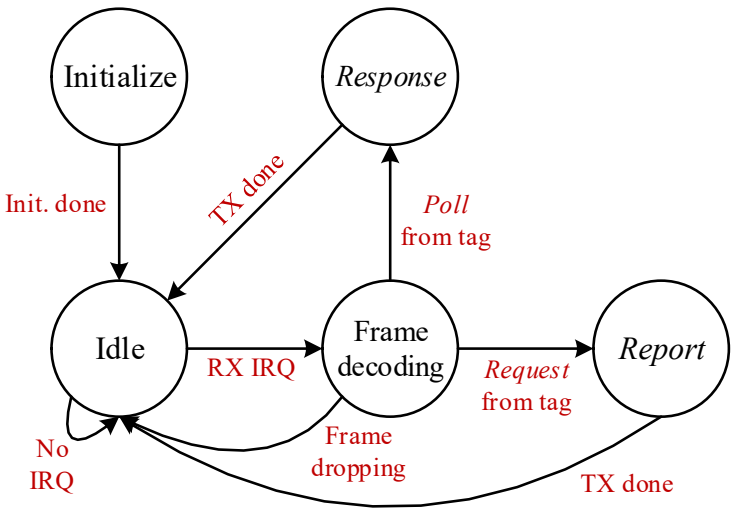

Figure 15. Anchor operation of DS-TWR+ represented with FSM state diagram.

Fig. 15 presents the anchor operation of DS-TWR+ with the FSM state diagram. First, the anchor initializes its configuration as a tag does. After the initialization is complete, the anchor enters the Idle state and waits for the RX IRQ generated by the *Poll* or *Request* reception from the tag. If RX IRQ occurs and a received frame is valid and not dropped, the anchor state becomes the frame decoding state. In this state, the next state transition is decided based on the mType in the decoded frame. When the message *Poll* from the tag arrives, i.e., mType is $AA_{(16)}$, the anchor immediately sends the message *Response* to the tag. However, when the message *Request* is received, i.e., mType is $CC_{(16)}$, the anchor estimates the distance between devices by using timestamps obtained from the tag, anchors both sides, and sends the message *Report* with the estimated distance. Subsequently, the anchor goes back to the Idle state and waits for the following message from the tag to be received.

For channel decoding, the UWB transceiver checks the error condition with the FCS delivered in every received frame and then generates RX IRQ. When the invalid FCS is detected, the device drops the received frame. In addition, when the frame belonging to another PAN arrives (invalid PAN ID) or the device address differs from the destination address of the received frame, the received frame is dropped.

It is expected that the message-exchange procedure of DS-TWR+ has to perform without the message frame loss, while the proposed UWB positioning system requires a tag and multiple anchors implemented with DS-TWR+. In this study, the anchors run without a specific transmission schedule because it passively operates according to the message from the tag. However, the tag requires the transmission

schedule to lead the message exchange. Fig. 16 presents the positioning schedule of the proposed UWB positioning system. In the active period during the total positioning time, the tag performs DS-TWR+ n times by updating the destination address according to the number of anchors (n) required for the tag localization observation. Hence, the active period is $T_{ac} = T_{TWR} \times n$, where T_{TWR} denotes the time duration required for the DS-TWR+ operation. After performing DS-TWR+ with the surrounding anchors, the tag is set to be inactive. In addition, the inactive period can be managed by increasing or decreasing the positioning interval time (T_s) defined as

$$T_{in} = T_s - T_{ac}, \tag{29}$$

where, T_{ac} and T_{in} represent the active and inactive periods, respectively. Finally, the tag repeats the active and inactive periods every T_s and increases fCnt. In this study, the host computer operates this timing schedule for EKF localization. For the multi-tag service, it can be beneficial to design time division multiple access or duty cycle limitation.

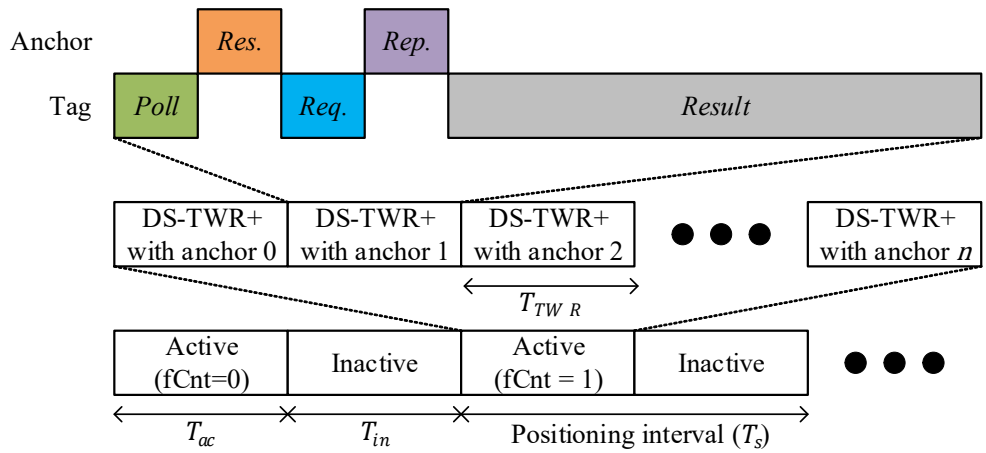

Figure 16. Positioning schedule of the proposed UWB positioning system.

B. AI Training and Inference

The AI inference phase in Fig. 9 performs channel classification based on the pre-trained LSTM network. In this thesis, the NLOS channel conditions were classified using an extensive dataset of TWRs. This dataset comprised TWR error and CIR data collected in various indoor environments with LOS and NLOS channel conditions. The UWB channels are divided into 10 levels based on deciles of TWR errors without any information on propagation conditions such as clutter, reflection, and through-the-wall.

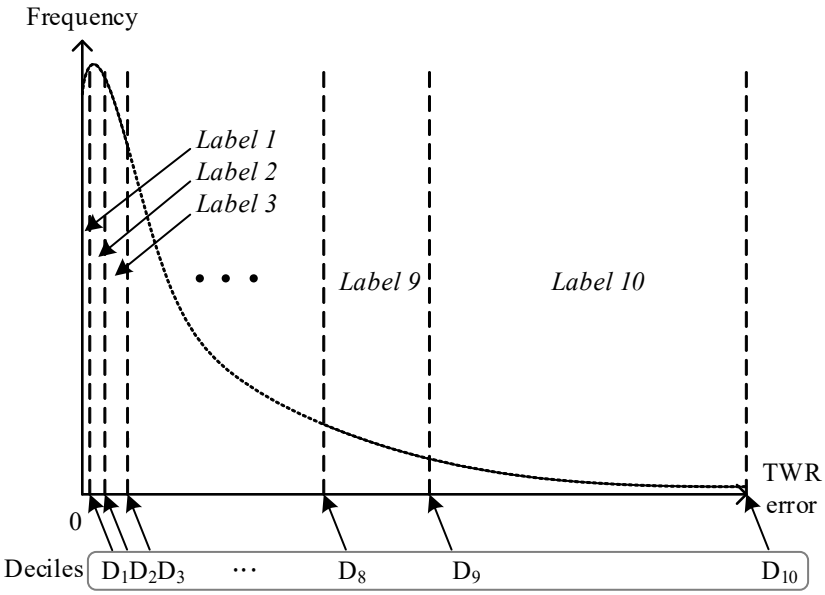

Figure 17. Labeling method for classification of NLOS channel conditions.

Fig. 17 presents the labeling of NLOS channel conditions denoted as deciles for TWR errors with the overall dataset as a population. The labels of channel conditions are determined by the deciles (D_1, D_2, ⋯, D_{10}) of the overall dataset.

The distribution information of TWR estimation errors from D_1 to D_{10} is presented in Table 3. Each labeled sample has the same data size equal to 10 % of the population set. In addition, the range of each label is increased exponentially because the TWR error is modeled by an exponential random variable. For example, the channel condition for Label 1 (top 10 % TWR accuracy) exhibits high precision in the narrow error range. Hence, it could belong to a clean LOS environment with the shortest direct path. However, Label 10 (bottom 10 % TWR accuracy) exhibits a low precision in the broad error range and is close to the extreme NLOS environment with severe biased error. In our training data set, Label 1 has an average error and error variance of 40 cm and 5.41e-4, respectively. However, an average error and error variance of Label 10 are 6.16 m and 0.58, respectively.

Table 3. Labeled dataset used for AI training, validation, and test.

Label (l)	**Deciles** (D_l) **[m]**	**Average error** ($\overline{DS_l}$) **[m]**	**Error variance** ($\hat{\sigma}_l^2$)	**Number of data**
1	0.078	0.0409	5.4144e-4	16,659
2	0.1503	0.1132	4.5576e-4	16,566
3	0.226	0.1851	4.5895e-4	16,787
4	0.315	0.2735	6.328e-4	16,618
5	0.4075	0.3598	7.0324e-4	16,624
6	0.576	0.4756	0.0023	16,683
7	1.3925	0.8949	0.0536	16,635
8	3.0809	2.2323	0.2634	16,678
9	5.1861	4.0329	0.3677	16,670
10	10.0107	6.1466	0.5819	16,662
Total		1.4755	3.9818	166,582

Before the LSTM training for the UWB channel classification operates, the labeled dataset was divided, as illustrated in Fig. 18, into training, validation, and test sets with 80 %, 10 %, and 10 % ratios, respectively. At each processing step, they were shuffled by normally distributed random numbers. The LSTM classification network was fit by a training dataset and evaluated by a validation set. In this work, the unbiased evaluation results obtained with the validation set were adopted to select the most suitable LSTM conditions and model hyperparameters.

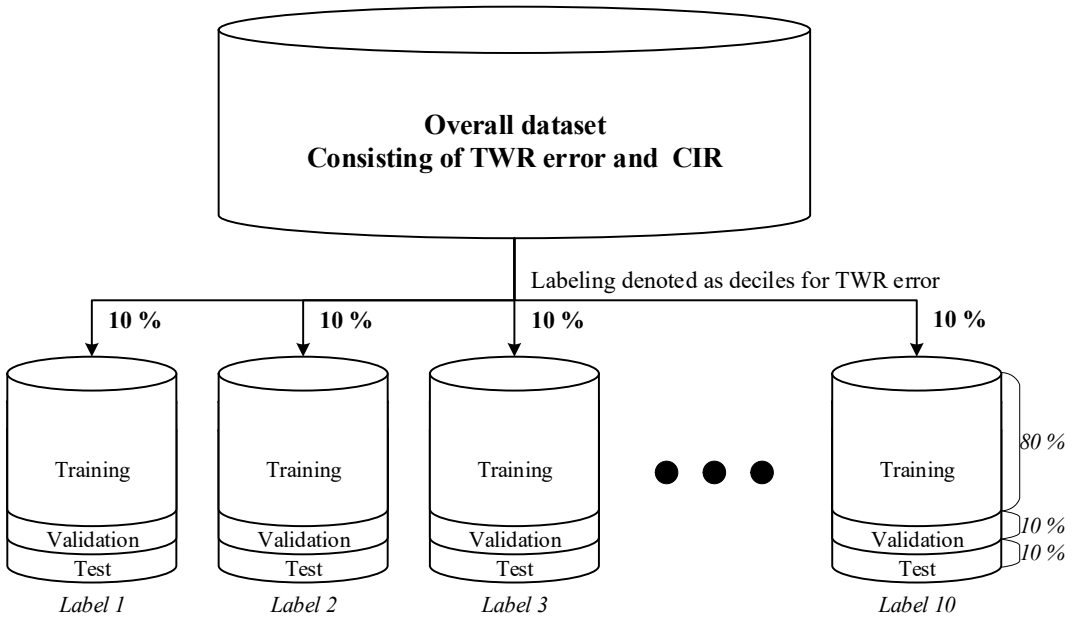

Figure 18. Split method in the labeled dataset.

Table 4 presents the designed models and their validation accuracies. For the model validation, the LSTM, bidirectional LSTM (Bi-LSTM) [63], and GRU [64] were compared. The input layer adopted a half-size CIR stream for AI training and inference, where the CIR samples were selected in Fig. 1 from 496 – 992 ns. Therefore, the length of the input sequence was 496 in the form of either the absolute of the CIR (CIR_{abs}) or raw CIR (CIR_{raw}) comprising the real and imaginary. Each RNN layer (LSTM, Bi-LSTM, and GRU) has hidden states of 496, same as the input sequence, and is connected to a dropout layer of 20 % to prevent the model from overfitting [65][66]. After the fully connected layer, it contains the softmax output layer for the channel condition classification. In our study, various models with a deeper network and half-reduced hidden units were evaluated, and the training time required to evaluate model complexity was measured for the epoch of 200 using the MATLAB deep learning training progress monitor [67]. Each model was evaluated with each learning process condition as follows: Adam optimizer, learning rate of 0.001 (constant), gradient threshold of 1, loss function of cross-entropy, iteration per epoch of 1041, and validation frequency of 8320 iterations.

Table 4. Validation accuracy for each RNN model.

Model	Input shape	RNN layers	Hidden units	Training time [min]	Overall accuracy [%]
1	CIR_{abs}	Single LSTM	248	130	53.79
2	CIR_{abs}	1st LSTM	248	211	79.85
		2nd LSTM	124		
3	CIR_{raw}	Single LSTM	248	129	63.65
4	CIR_{raw}	1st LSTM	248	210	82.15
		2nd LSTM	124		
5	CIR_{raw}	1st LSTM	248	270	82.02
		2nd LSTM	124		
		3rd LSTM	62		
6	CIR_{raw}	1st LSTM	248	322	82.01
		2nd LSTM	124		
		3rd LSTM	62		
		4th LSTM	31		
7	CIR_{raw}	Single Bi-LSTM	248	223	62.61
8	CIR_{raw}	1st Bi-LSTM	248	593	81.05
		2nd Bi-LSTM	124		
9	CIR_{raw}	Single GRU	248	124	65.86
10	CIR_{raw}	1st GRU	248	202	79.68
		2nd GRU	124		

As presented in the validation result, Models 1 and 2 using the input shape of CIR_{abs} defined as CIR magnitude exhibited partially divergent accuracy and loss in the training progress. They had validation accuracy lower than Models 3 and 4 using the same LSTM model because they excluded phase information of CIR signal at the model training. Hence, Models 1 and 2 were unsuitable for the proposed system. Models 3, 7, and 9 designed by a single RNN layer did not achieve validation accuracy above 80 %. This implies that the proposed method requires deeper neural networks for channel condition classification. In contrast, the models stacked with two or more RNN layers achieved an 80 % level of validation accuracy. However, Models 5, 6, and 8 spent more training time than

Model 4. Among these models, although Model 8 using the Bi-LSTM spent the longest training time of 593 min at the AI server used for the AI training in this study. It exhibited a similar performance of the accuracy of 80 % level. It could mean that there is no beneficial information in the backward sequence of the CIR. However, Model 10 using double GRU layers exhibited a validation accuracy close to 80 % and required a short training time of 202 min because of its lightweight design. However, it still exhibited lower performance than Model 4 using double LSTM layers that required an additional time of 8 min. Model 4 achieved an overall accuracy of 82.15 % with a training time of 210 min. Moreover, it exhibited a fast model convergence than more complex Models 5, 6, and 8. Finally, Model 4 was selected for the proposed system because of its superior classification performance and efficient training time. Subsequently, the Model 4 trained labels for channel classification was pre-deployed for the NLOS mitigation phase in the host computer.

C. NLOS Mitigation

In the AI inference phase, the pre-trained model (stacked-LSTM classification network) predicts channel condition with a label number for each DS-TWR+ result. Subsequently, the NLOS mitigation phase adopts these classified labels for generating NLOS mitigated measurements. In this thesis, the statistics of the dataset were used to approximate NLOS errors [44]. It was assumed that there was an NLOS-biased error b_{nlos} in the labeled dataset, and it could be modeled by the average error of its dataset [68]. In this step, the measurement noise covariance matrix R was updated using the variance of the labeled dataset because the performance of TWR varies with the change in the NLOS channel [69]. Hence, the NLOS mitigated measurement $\hat{\mathrm{Z}}_k$ and its noise covariance matrix $\hat{\mathrm{R}}_k$ at the time step k, classified label l, and anchor number n are expressed as:

$$\hat{\mathrm{Z}}_k = \begin{bmatrix} d_{0k} - \overline{DS_{0l}} + v_{0k} \\ d_{1k} - \overline{DS_{1l}} + v_{1k} \\ d_{2k} - \overline{DS_{2l}} + v_{2k} \\ \vdots \\ d_{nk} - \overline{DS_{nl}} + v_{nk} \end{bmatrix}, \tag{30}$$

$$\hat{\mathrm{R}}_k = diag(\hat{\sigma}_{0l}^2, \hat{\sigma}_{1l}^2, \hat{\sigma}_{2l}^2, \cdots, \hat{\sigma}_{nl}^2), \tag{31}$$

where $\overline{DS_{nl}}$ and $\hat{\sigma}_{nl}^2$ denote the average error and error variance of the labeled dataset, respectively. Finally, the determined $\hat{\mathrm{Z}}_k$ and $\hat{\mathrm{R}}_k$ were used as Z_k and R_k of the correction phase of Fig. 7.

IV. Experimental Setup

This section introduces the testbed of the proposed UWB positioning system in a typical indoor environment and describes the dataset and its collection method.

A. Testbed Setup

The tag device of the proposed system comprises three modules, as illustrated in Fig. 19. In this study, the UWB, microcontroller unit, and data transfer modules used were DWM1000, LPC1768, and FT232H, respectively. LPC1768 and FT232H can transfer ranging results and its CIR stream of 1984 bytes to the host computer using 6 Mbps serial communication.

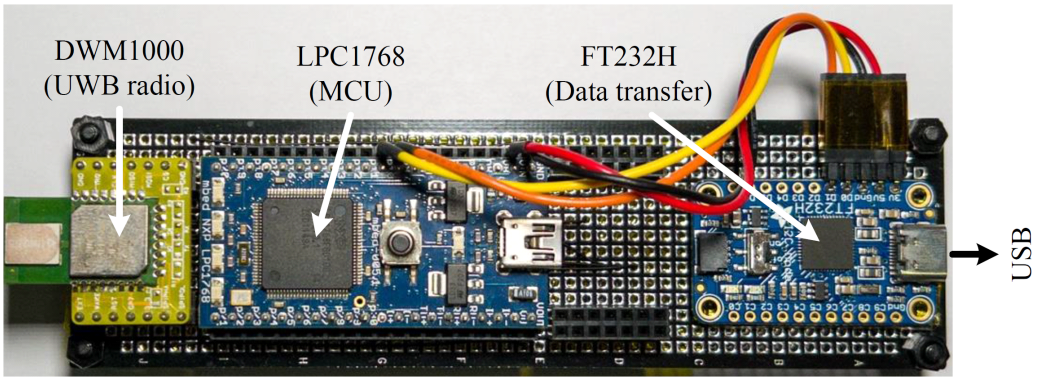

Figure 19. Main modules of tag device.

The anchors used in this study were DWM1001-DEV devices manufactured by Decawave. These devices were reprogrammed to work as DS-TWR+ anchors. In addition, the parameters of UWB positioning were configured as denoted in Table 5.

Table 5. Parameter configuration of the UWB system.

Parameter	Value	Parameter	Value
Channel	3	Bandwidth	499.2 [MHz]
Data rate	110 [Kbps]	Pulse repetition frequency (PRF)	16 [MHz]
Preamble length	1024	Preamble code	5
Operation time of DS-TWR+ (T_{TWR})	25 [ms]	Positioning interval (T_s)	200 [ms]

The AI server performed AI training, validation, and test using MATLAB 2021a of Mathworks [67]. Its specifications are presented in Table 6. In addition, the host computer illustrated in Fig. 8 performed AI-EKF localization. Its specifications are as follows: CPU of Intel i7 10875H, GPU of Nvidia RTX 2060, and RAM of 32GB.

Table 6. AI server configuration and its framework.

Category	Tool
CPU	AMD Ryzen 7 5800X @ 3.8 GHz
GPU	Nvidia GeForce GTX 3080 10 GB @ 8704 CUDAs
RAM	DDR4 32 GB @ 3600 MHz
Operating system	Windows 10 Education
AI framework	Deep learning toolbox, parallel computing toolbox, statistics and machine learning toolbox of MATLAB 2021a

B. Dataset Setup

The experimental area for data collection was a typical indoor environment on the 8th floor, college of IT convergence, Chosun University, in KOREA, as illustrated in Fig. 20. Data collection was performed at four sub-areas from (a) to (d).

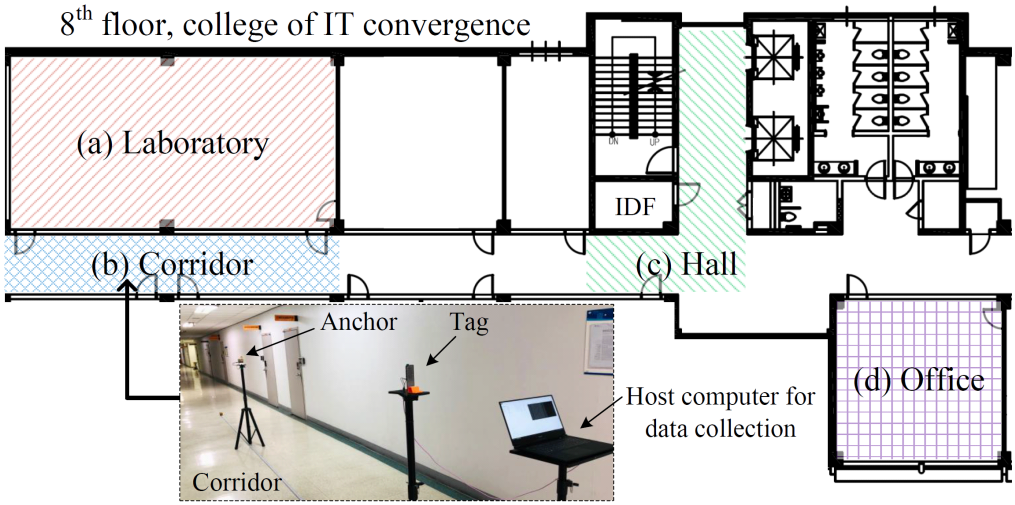

Figure 20. Experimental area for the data collection.

Sub-area (a) was a laboratory with tables and experimental devices such as a multimeter, oscilloscope, power supply, and function generator. Sub-area (b) was a corridor without obstacles. The picture in Fig. 20 expresses data collection in this sub-area. Fig. 21 presents the DS-TWR+ testbed tag and anchor positions for the data collection in sub-areas (a) and (b). In sub-area (a), the tag was located at T0 and T1, and the anchor was installed on black dots. The distance between positions for each device to be located was 2 m in width and 2.925 m in height. In

sub-area (b), the tag positions were M0 and M1, and the locations of the anchor were on each black dot in the corridor. The distance intervals of each device were 2 m in width and 0.67 m in height. The tag in sub-area (a) could measure the through-the-wall propagation effect of the UWB signal transferred from sub-area (b). In this collection, the tag obtained DS-TWR+ data at T0 and T2 when the anchor was placed on one of M0, M1, and black dots in sub-area (b).

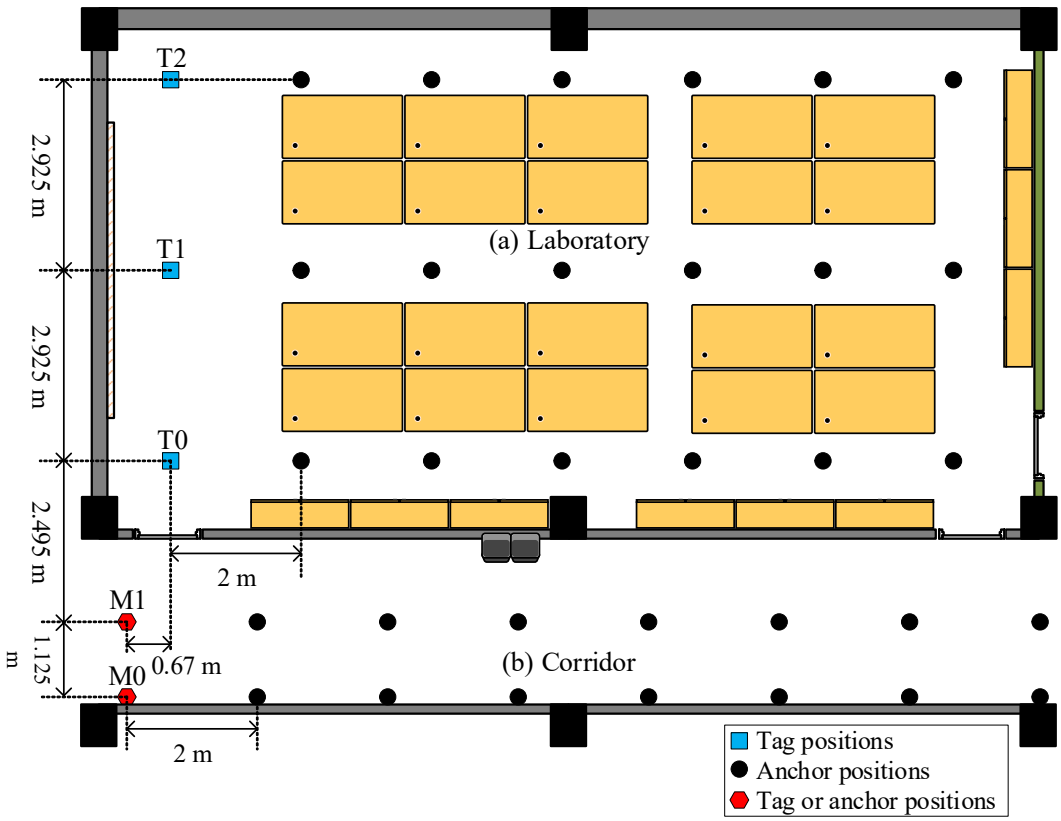

Figure 21. Sub-areas (a) and (b) with tag and anchor positions for the data collection.

Sub-area (c) was a hall with a corner, as illustrated in Fig. 22. Anchor positions were between the stair and elevator, while tag positions were in front of the office. This placement of the testbed tag and anchor generated the NLOS channel.

Significantly, the space of the intermediate distribution frame (IDF) adopted for cross-connecting ethernet cables was located in this corner, which created an extreme NLOS path. In sub-area (c), the distance interval of the tag was 1.8 m in width, while the distance intervals of the anchor were 0.9 m in width and 1.8 m in height.

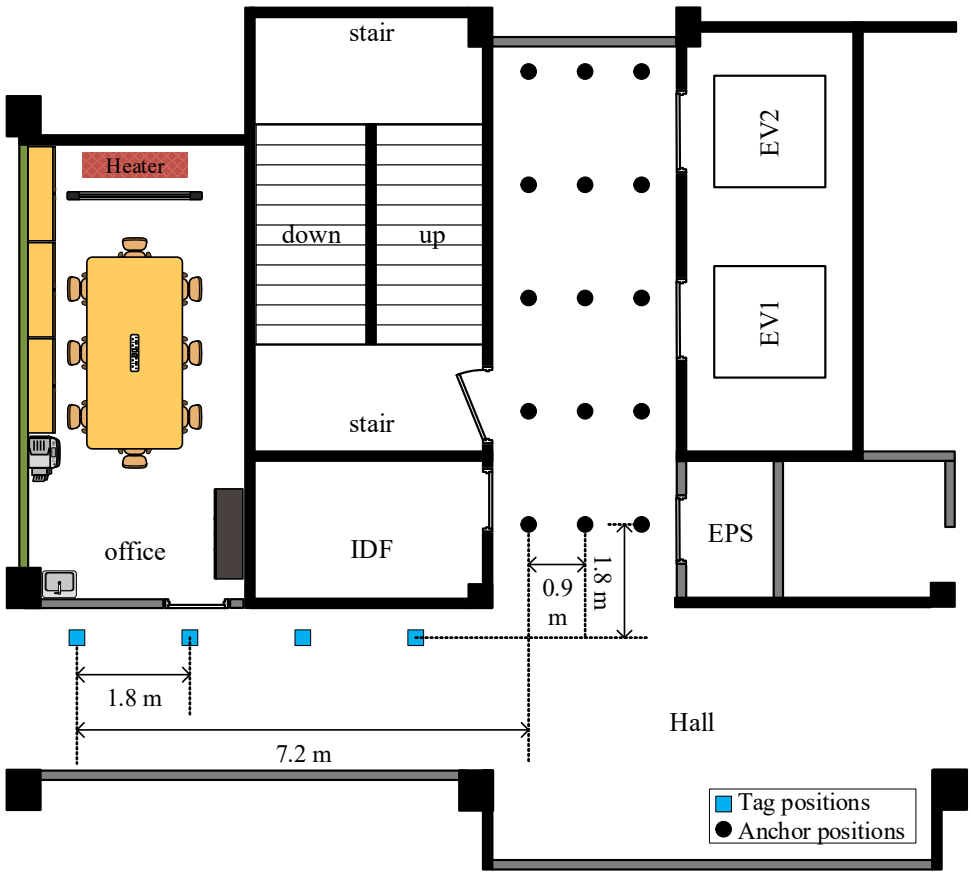

Figure 22. Sub-area (c) with tag and anchor positions for the data collection.

Sub-area (d) shown in Fig. 23 was a common office area with partitions, PCs, monitors, and office furniture. This sub-area contained a higher density of obstacles than other sub-areas. Thus, the occurrence of LOS channels was limited, and

multipath propagation was primarily observed. In this sub-area, anchor positions were also on the black dots. The distance interval of the tag was 1.8 m in width, while the distance intervals of the anchor were 5.4 m in width and 2.25 m and 5.4 m in height.

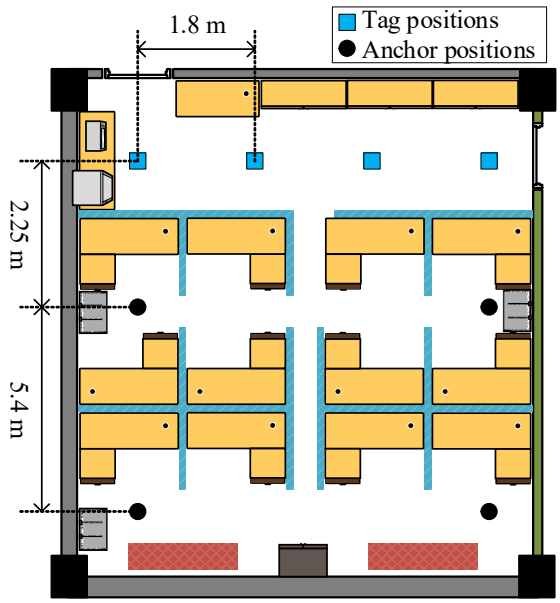

Figure 23. Sub-area (d) with tag and anchor positions for the data collection.

For the data collection at each sub-area, the tag and anchors moved with a uniform distance interval, and the tag at each measurement point stored the measured 500 DS-TWR+ distance estimation results without human interference and another 500 results with human interference. Hence, this collecting method could enable the application of the human body impact to the AI model [70]. Finally, outlier removal was performed from the collected TWR error based on a standard deviation of 3 [71]. Table 3 presents the labeled dataset measured in the experimental area for UWB channel classification.

C. Scenario Setup

Two types of experimental scenarios were set up to evaluate the performance of the proposed UWB positioning system, as illustrated in Fig. 24. The first scenario, KNOWN, which employs the same places from the training set, was obtained for the AI-EKF performance test. It was performed in a laboratory and corridor separated by the wall on the 8th floor used in the data collection area. The other scenario, UNKNOWN, which adopts different locations from the training set, was obtained for the AI-EKF performance evaluation at another office and corridor separated by tempered glass on the 2nd floor of the same building. At this location, the corridor had an open space expanded on the 2nd floor. The 2nd scenario, UNKNOWN, was designed for a fair evaluation of the AI approach because AI-EKF was one of supervised learning.

(a)

(b)

Figure 24. Location of experimental scenarios for the performance evaluation of the proposed UWB positioning system: (a) scenario KNOWN on the 8th floor (b) scenario UNKNOWN on the 2nd floor.

For the performance evaluation, as illustrated in Fig. 25 and 26, indoor maps of the experimental scenarios and their reference points were created, with which the tag positions were estimated. Tables 7, 8, 9, and 10 present the coordinates of the reference points. In addition, the tags and anchors were placed at a height of 1.5 m.

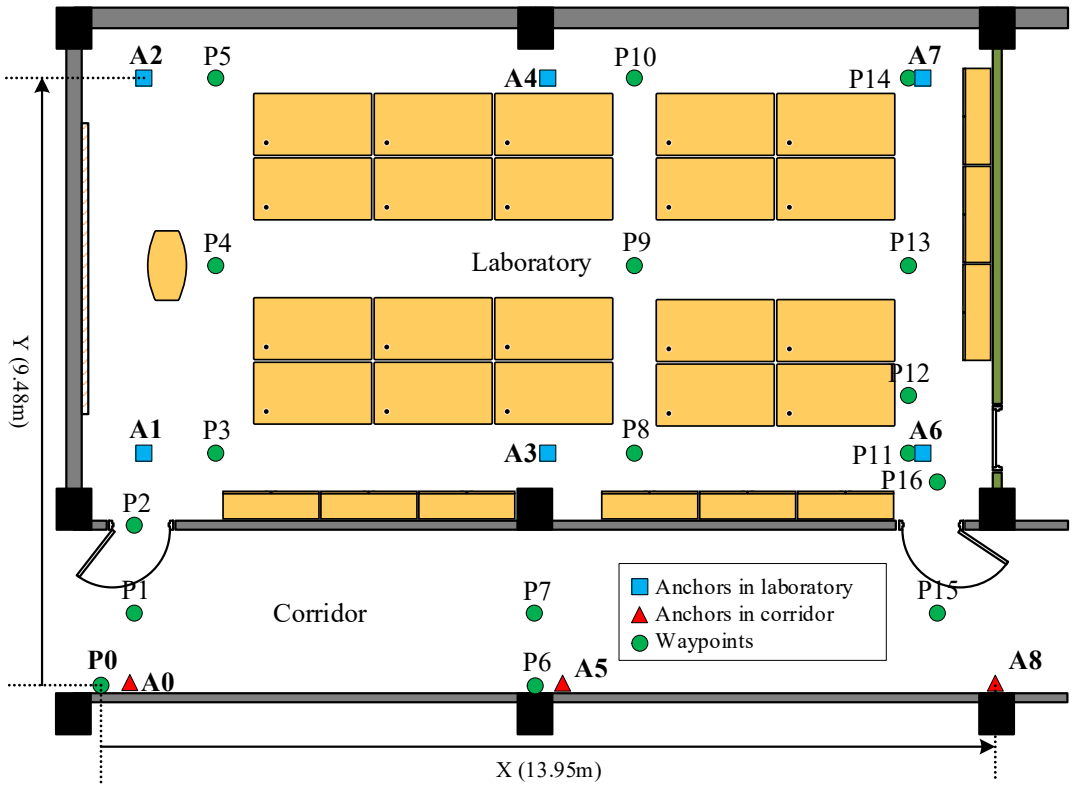

Figure 25. Indoor map with reference points and anchors in scenario KNOWN.

Table 7. Coordinates of anchors in scenario KNOWN.

Anchor	Coordinates (x, y) [m]	Anchors	Coordinates (x, y) [m]	Anchors	Coordinates (x, y) [m]
A0	0.45, 0	A1	0.67, 3.62	A2	0.67, 9.47
A3	6.97, 3.62	A4	6.97, 9.47	A5	7.2, 0
A6	12.82, 3.62	A7	12.82, 9.47	A8	13.95, 0

Table 8. Coordinates of reference points in scenario KNOWN.

Ref.	Coordinates (x, y) [m]	Ref.	Coordinates (x, y) [m]	Ref.	Coordinates (x, y) [m]
P0	0, 0	P1	0.52, 1.125	P2	0.52, 2.4
P3	1.79, 3.62	P4	1.79, 6.545	P5	1.79, 9.47
P6	6.6, 0	P7	6.6, 1.125	P8	8.32, 3.62
P9	8.32, 6.545	P10	8.32, 9.47	P11	12.595, 3.62
P12	12.595, 4.52	P13	12.595, 6.545	P14	12.595, 9.47
P15	13.045, 1.125	P16	13.045, 3.17	-	-

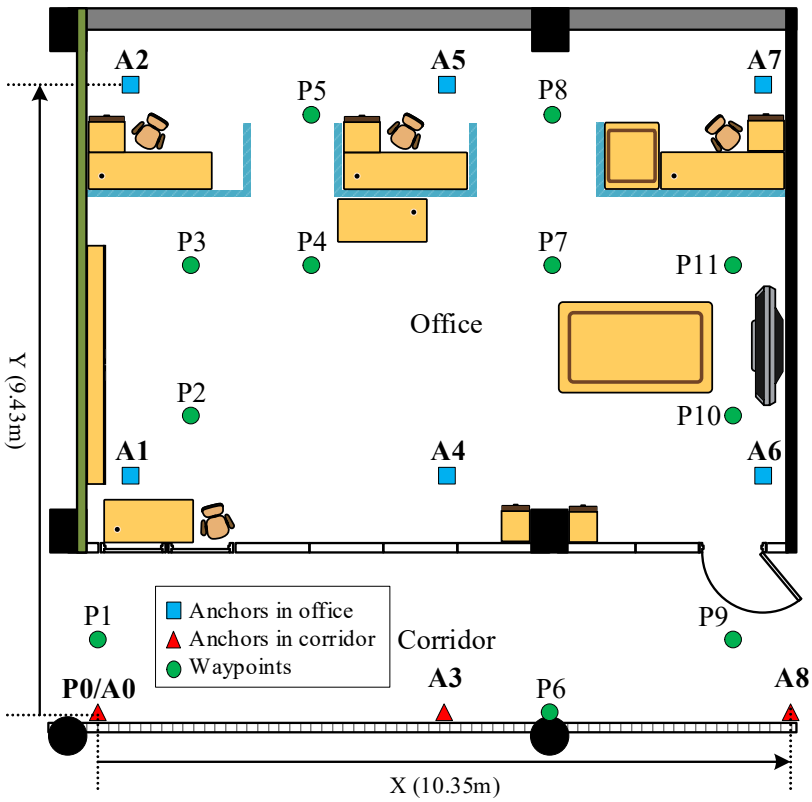

Figure 26. Indoor map with reference points and anchors in scenario UNKNOWN.

Table 9. Coordinates of anchors in scenario UNKNOWN.

Anchor	Coordinates (x, y) [m]	Anchors	Coordinates (x, y) [m]	Anchors	Coordinates (x, y) [m]
A0	0, 0	A1	0.49, 3.58	A2	0.49, 9.43
A3	5.175, 0	A4	5.215, 3.58	A5	5.215, 9.43
A6	9.94, 3.58	A7	9.94, 9.43	A8	10.35, 0

Table 10. Coordinates of reference points in scenario UNKNOWN.

Ref.	Coordinates (x, y) [m]	Ref.	Coordinates (x, y) [m]	Ref.	Coordinates (x, y) [m]
P0	0, 0	P1	0, 1.125	P2	1.39, 4.48
P3	1.39, 6.73	P4	3.19, 6.73	P5	3.19, 8.98
P6	6.75, 0	P7	6.79, 6.73	P8	6.79, 8.98
P9	9.49, 1.125	P10	9.49, 4.48	P11	9.49, 6.73

In addition, three different routes and two anchor deployments were generated for each scenario, as presented in Tables 11 and 12, and the AI-EKF method was compared with the proposed UWB positioning system and existing positioning methods such as LS, WLS, and EKF without AI approaches. For the comparison, the Q values of EKF and AI-EKF were set as $diag(0.01, 0.01)$, and R of EKF was configured with $diag(0.01, \cdots, 0.01)$ for four and five anchors, respectively.

Table 11. Waypoints of each trajectory used in the scenario.

Map	Route	Waypoints
Scenario KNOWN (8th floor)	Laboratory	P5⇒P4⇒P9⇒P8⇒P11⇒P14
	Corridor	P1⇒P6⇒P15
	Both	P1⇒P15⇒P16⇒P11⇒P14⇒P10⇒P9⇒P4⇒P3⇒P2⇒P1
Scenario UNKNOWN (2nd floor)	Office	P2⇒P3⇒P4⇒P5⇒P8⇒P7⇒P11⇒P10
	Corridor	P1⇒P6⇒P9
	Both	P1⇒P9⇒P10⇒P2⇒P7

Table 12. Anchor deployment used in the scenario.

Map	Number of anchors	Anchor deployment
Scenario KNOWN (8th floor)	4	A1, A4, A5, A6
	5	A0, A2, A3, A7, A8
Scenario UNKNOWN (2nd floor)	4	A1, A3, A5, A6
	5	A0, A2, A4, A7, A8

V. Performance Evaluation

A. NLOS Classification Performance

Fig. 27 presents a confusion matrix evaluated with the test set to provide the classification performance of the proposed LSTM model shown in Fig. 9. In this figure, the target class is the actual label of the test dataset, while the output label is the predicted label of the proposed model. For each label, the column on the far right expresses precision and false discovery rate (FDR), while the row at the bottom denotes recall and false-negative rate (FNR). In this evaluation, an overall accuracy of 81.7 % was achieved, and the FDR and FNR for each label mainly occurred for adjacent labels. It is clear that the selected model can be beneficial to the UWB channel classification for the proposed UWB positioning system. For example, when the actual channel condition is a clear LOS indicated as Label 1 or 2, but the proposed LSTM model infers channel condition as Label 9 or 10, the proposed UWB positioning system excludes this distance measurement because of its significant variance. Hence, it triggers the performance degradation of positioning. In another case, the selected model predicts channel class as Label 1 or 2, but the actual channel is the NLOS indicated as Label 9 or 10. The proposed UWB positioning system primarily adopts this measurement because of its slight variance. Therefore, its positioning performance deteriorates. Unlike the example, the selected LSTM model mainly inferred correct channel conditions and selected the adjacent labels even in the worse cases. In other words, even though there is an incorrect inference, the selected model can be beneficial in improving positioning performance.

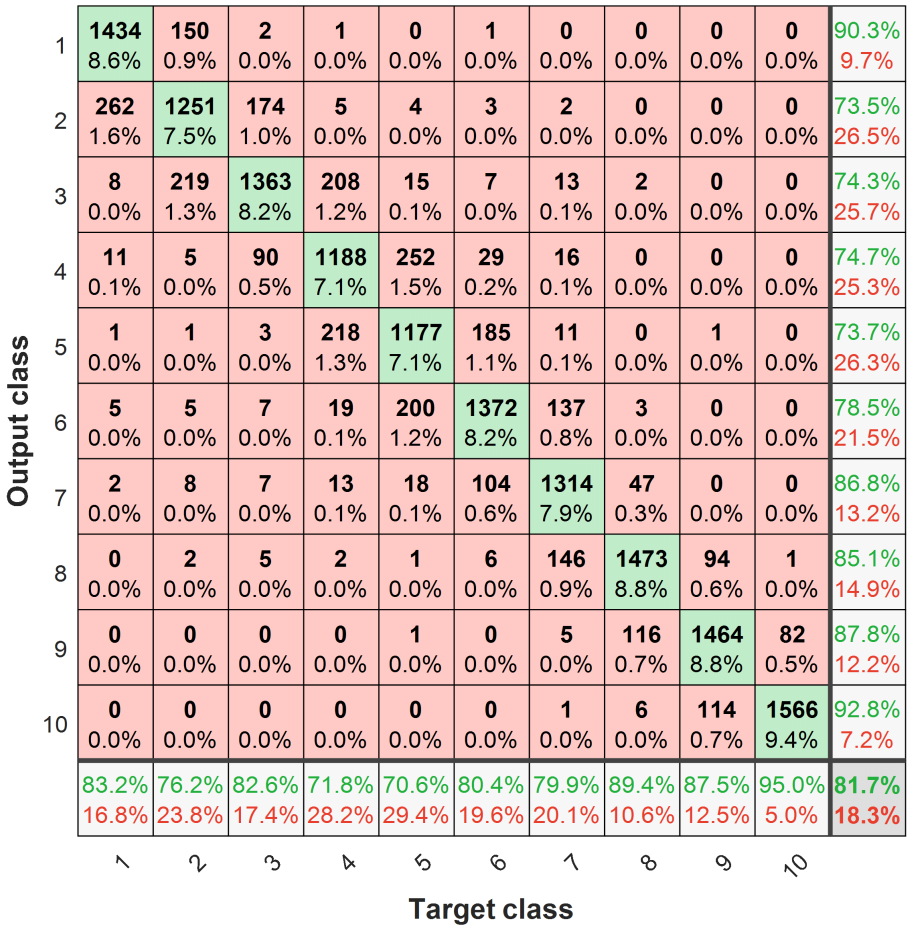

Figure 27. Classification performance of the proposed LSTM network.

B. Positioning Performance

This section provides the positioning performance of the proposed system for each scenario with a 2D trajectory in terms of the cumulative distribution function (CDF) of positioning errors, root mean square error (RMSE), and standard deviation (STD) of the positioning errors.

1) Scenario KNOWN Using Four Anchors

Fig. 28, 29, and 30 present trajectories and CDFs of positioning errors for each method in the scenario KNOWN using four anchors. Furthermore, Tables 13 and 14 express RMSE and STD of positioning errors measured for each method under the same condition. In this scenario, three anchors (A1, A4, and A6) were installed in the laboratory, and an anchor A5 was installed the corridor. Therefore, channel conditions in the laboratory (sub-area (a)) generated by anchors A1, A4, and A6 were better than those generated by A5 located in the corridor. However, in the corridor route, anchors located in the corridor provided more favorable channel conditions than others. Among the existing positioning approaches, WLS achieved 8.5 % RMSE improvement on average for each trajectory over LS because its adaptive weight based on distance proximity exerted a higher impact on the anchors within the same area in each experimental path. In addition, WLS achieved an average precision improvement of 70.5 % over LS. In contrast, EKF generated biased trajectories because of NLOS error. It performed similar to WLS, with an 8.4 % RMSE improvement on average compared to LS. However, it achieved an average precision enhancement of 158.1 % over LS because of its noise reduction ability. In contrast, AI-EKF obtained precise trajectories at every route without biased error. Moreover, it corrected the trajectory fluctuation around P2 and P16. In this zone, several anchors were located behind the pedestrian's handheld tag, and steel doors, walls, and furniture were located near the tags. Therefore, the furnishing in this zone exhibited an adverse effect on the positioning performance. Although LS, WLS, and EKF generated unstable and biased trajectories, AI-EKF improved the positioning accuracy and precision by an average RMSE of 66.4 % and an average STD of 199.1 % compared to LS.

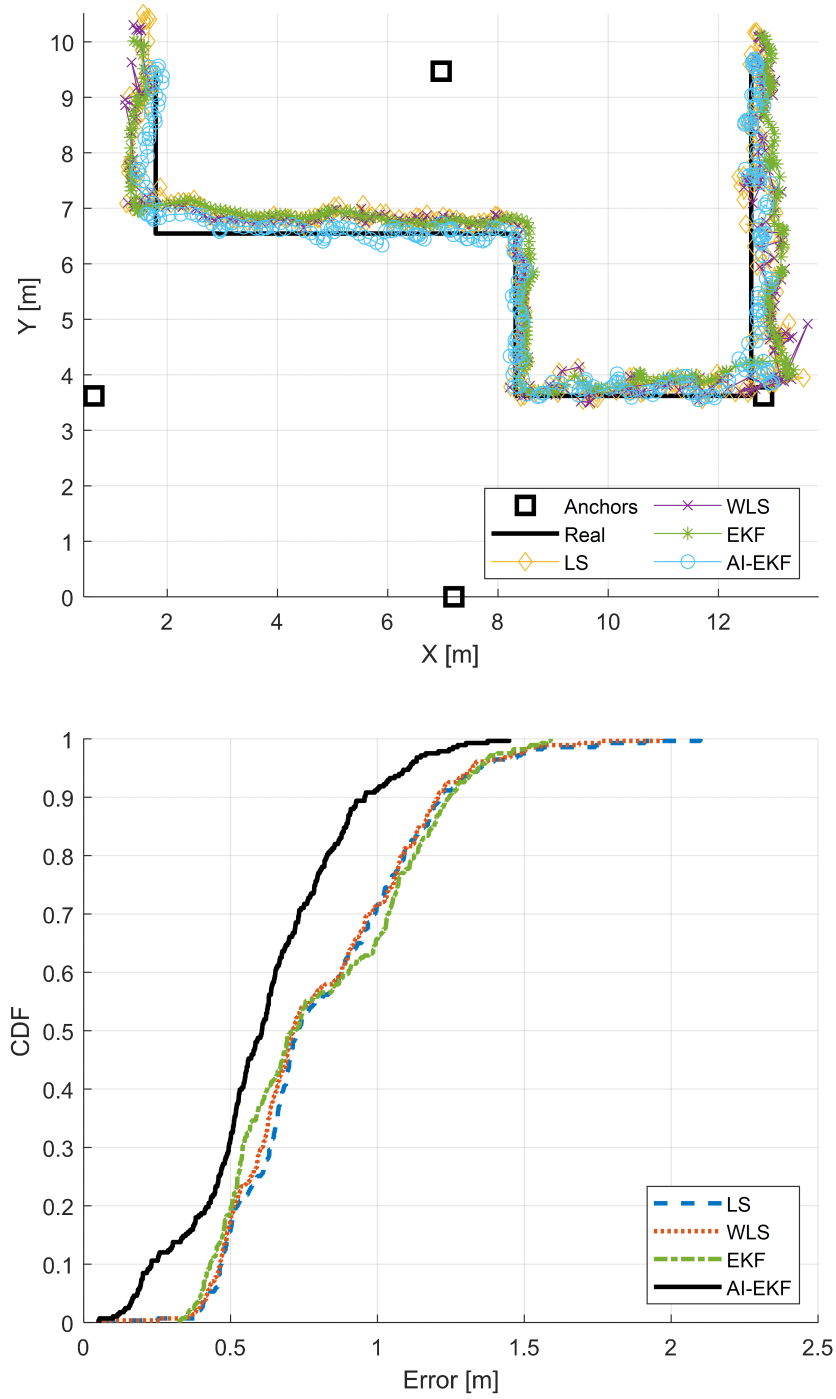

Figure 28. Trajectories (top) and positioning error CDFs (bottom) measured by each method in the laboratory on the 8th floor using four anchors.

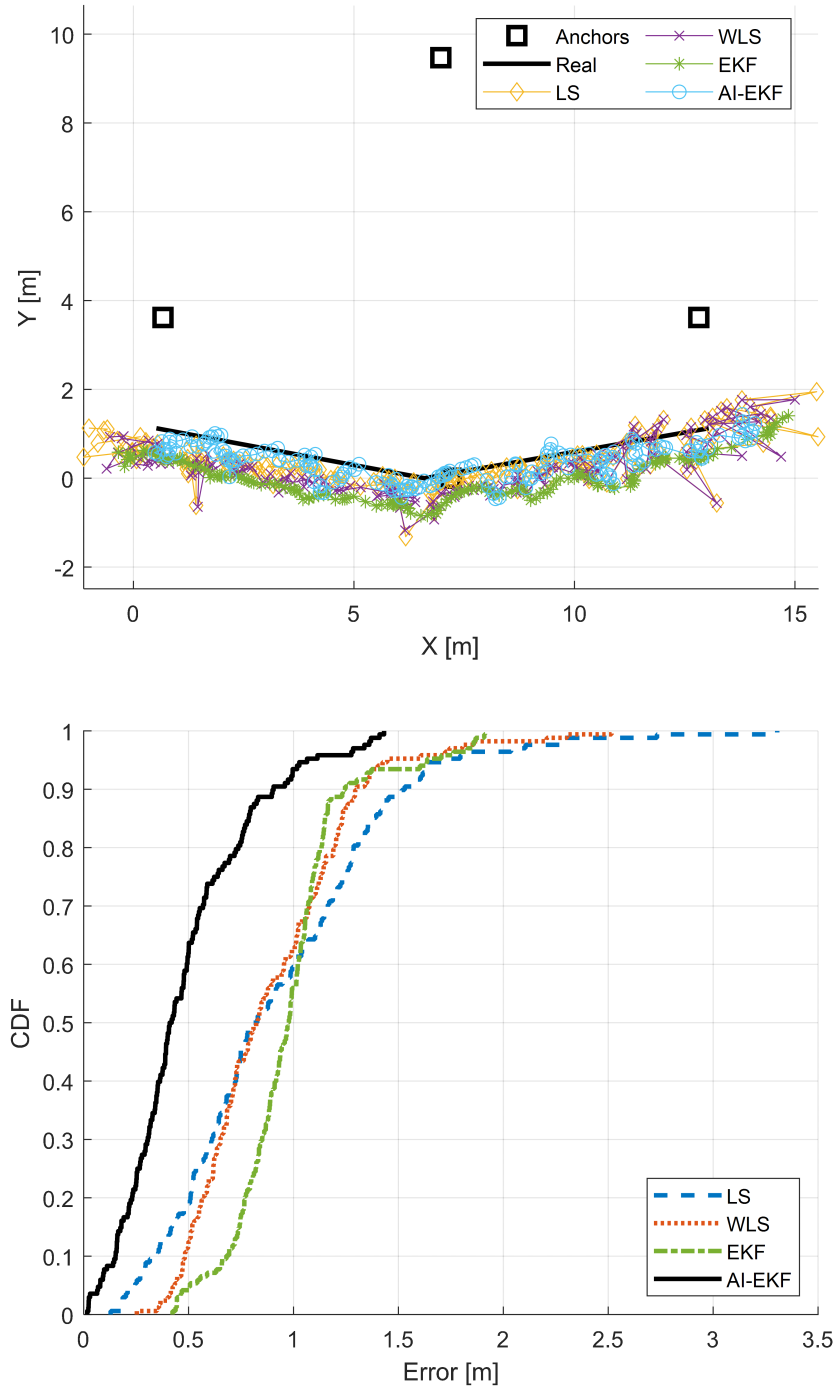

Figure 29. Trajectories (top) and positioning error CDFs (bottom) measured by each method in the corridor on the 8th floor using four anchors.

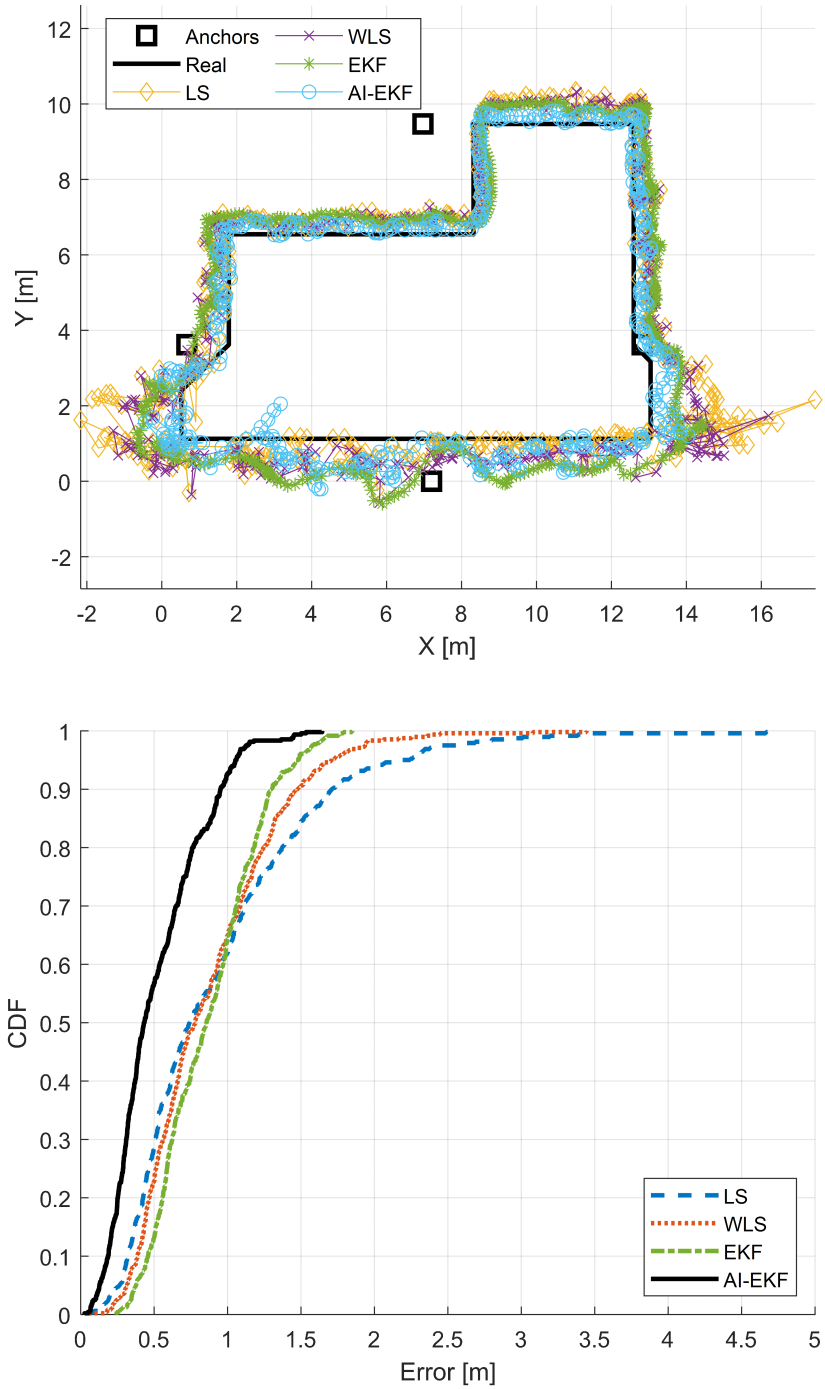

Figure 30. Trajectories (top) and positioning error CDFs (bottom) measured by each method in both the laboratory and corridor on the 8th floor using four anchors.

Table 13. RMSE of positioning results at each method in scenario KNOWN using four anchors.

Methods	Laboratory [m]	Corridor [m]	Both [m]
LS	0.8782	1.0519	1.1309
WLS	0.8609	0.9708	0.9903
EKF	0.8656	1.0248	0.9341
AI-EKF	0.6719	0.5712	0.5968

Table 14. STD of positioning errors at each method in scenario KNOWN using four anchors.

Methods	Laboratory	Corridor	Both
LS	0.0968	0.2589	0.4142
WLS	0.0938	0.1427	0.2151
EKF	0.102	0.083	0.1133
AI-EKF	0.0707	0.0953	0.0914

2) Scenario KNOWN Using Five Anchors

Fig. 31, 32, and 33 present trajectories and CDFs of positioning errors for each method in the scenario KNOWN using five anchors. Furthermore, Tables 15 and 16 present the RMSE and STD of positioning errors measured for each method under the same condition. Fig. 34 presents the average RMSE and STD for routes of each method. In this scenario, three anchors (A2, A3, and A7) were installed in the laboratory, while two anchors (A0 and A8) were installed in the corridor. Therefore, channel conditions in the laboratory (sub-area (a)) generated by anchors A2, A3, and A7 were better than those generated by A0 and A8 in the corridor. However, in the corridor route, anchors located in the corridor provided more favorable channel conditions than others. Similar to the results of the scenario using four anchors, WLS achieved an average 16.8 % RMSE improvement for each trajectory over LS. In addition, WLS achieved an average precision improvement of 55.2 % over LS. In contrast, EKF generated biased trajectories because of the NLOS error. It performed worse than WLS, with an average 10 % RMSE improvement compared to LS. However, it achieved an average precision enhancement of 166.8 % over LS. Although LS, WLS, and EKF generated unstable and biased trajectories, AI-EKF improved the positioning accuracy and precision by an average RMSE of 112.7 % and an average STD of 368 % compared to LS.

In this scenario, the additional anchor deployed at the corridor enhanced the positioning performance. As illustrated in Fig. 34, LS, WLS, EKF, and AI-EKF achieved average RMSEs of 41.6 %, 52.5 %, 43.7 %, and 81.1 % improvements, respectively; also, each method enhanced average STD of 105.4 %, 86.9 %, 112.3 %, and 221.3 %, respectively, compared with the case of the four anchors.

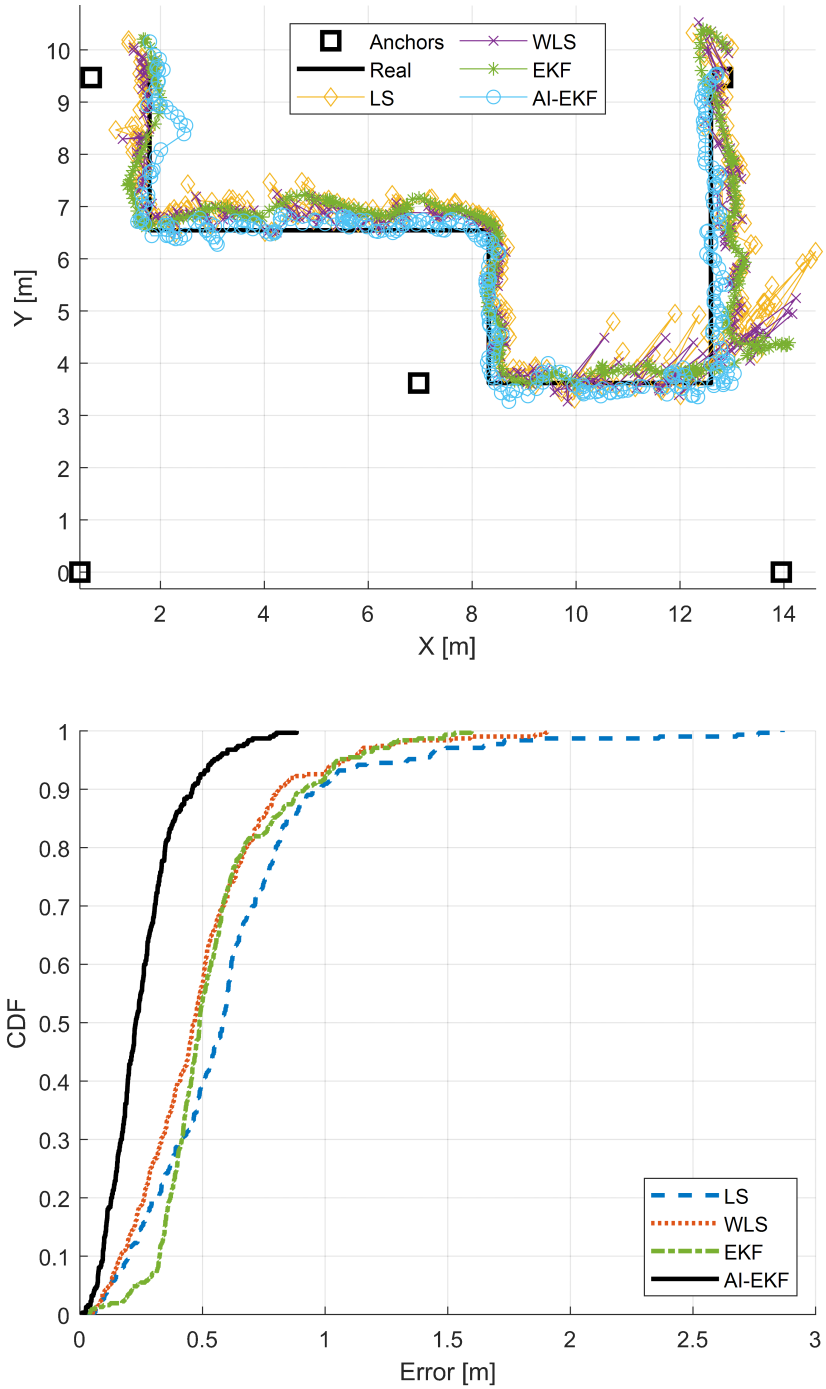

Figure 31. Trajectories (top) and positioning error CDFs (bottom) measured by each method in the laboratory on the 8th floor using five anchors.

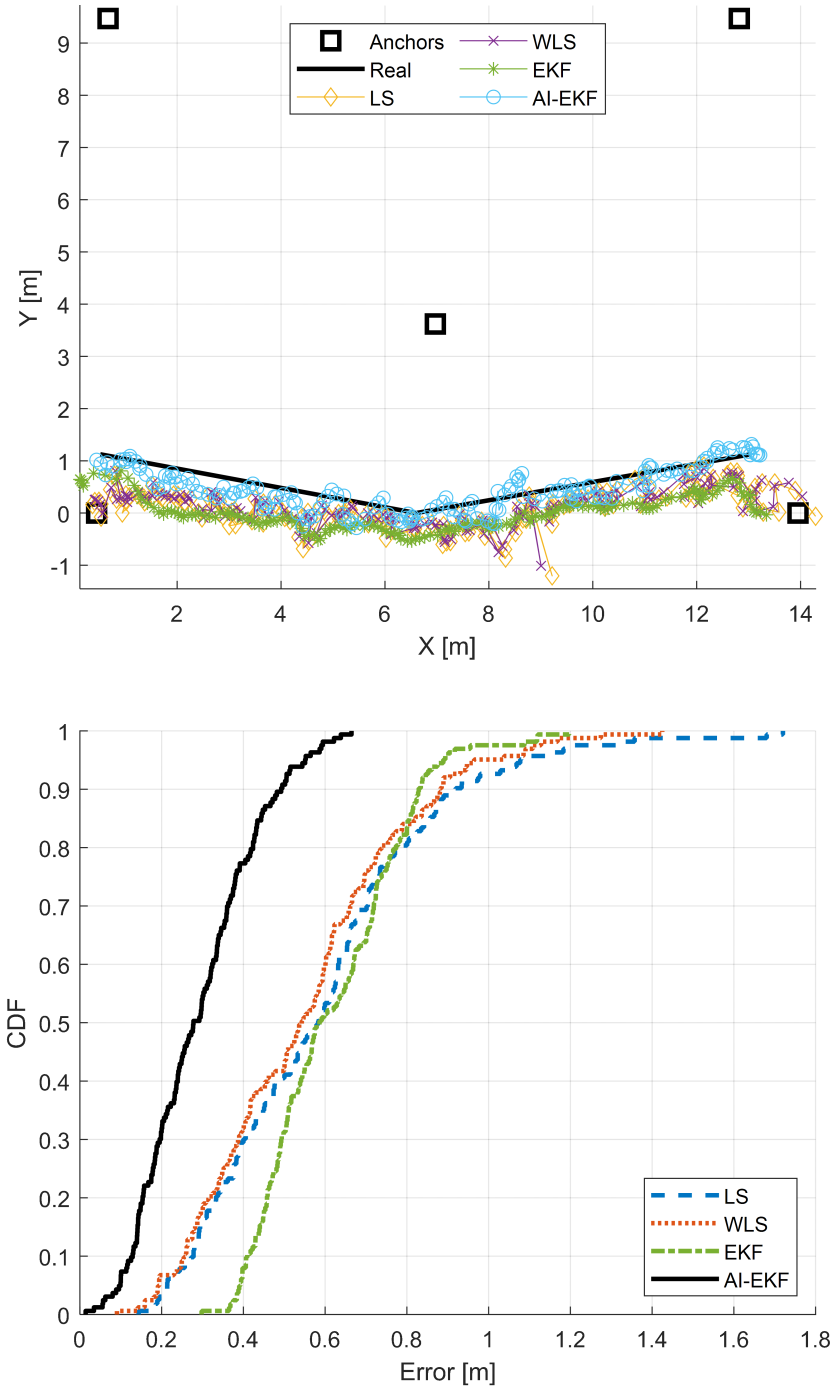

Figure 32. Trajectories (top) and positioning error CDFs (bottom) measured by each method in the corridor on the 8th floor using five anchors.

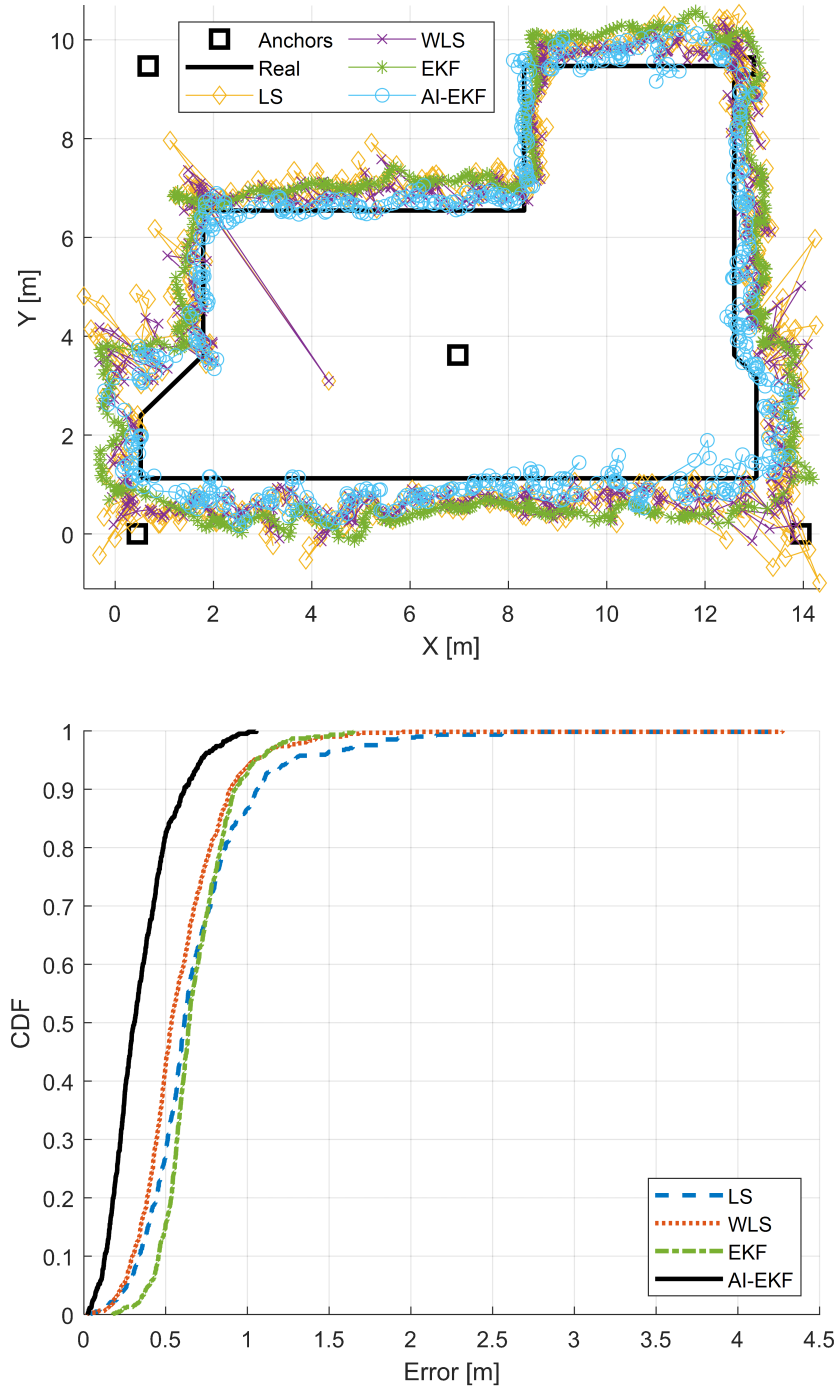

Figure 33. Trajectories (top) and positioning error CDFs (bottom) measured by each method in both the laboratory and corridor on the 8th floor using five anchors.

Table 15. RMSE of positioning results at each method in scenario KNOWN using five anchors.

Methods	Laboratory [m]	Corridor [m]	Both [m]
LS	0.7266	0.653	0.7822
WLS	0.582	0.6058	0.6627
EKF	0.607	0.6431	0.7149
AI-EKF	0.297	0.3241	0.3951

Table 16. STD of positioning errors at each method in scenario KNOWN using five anchors.

Methods	Laboratory	Corridor	Both
LS	0.1561	0.0787	0.1401
WLS	0.0896	0.0628	0.0892
EKF	0.0665	0.0296	0.0444
AI-EKF	0.0228	0.0199	0.0374

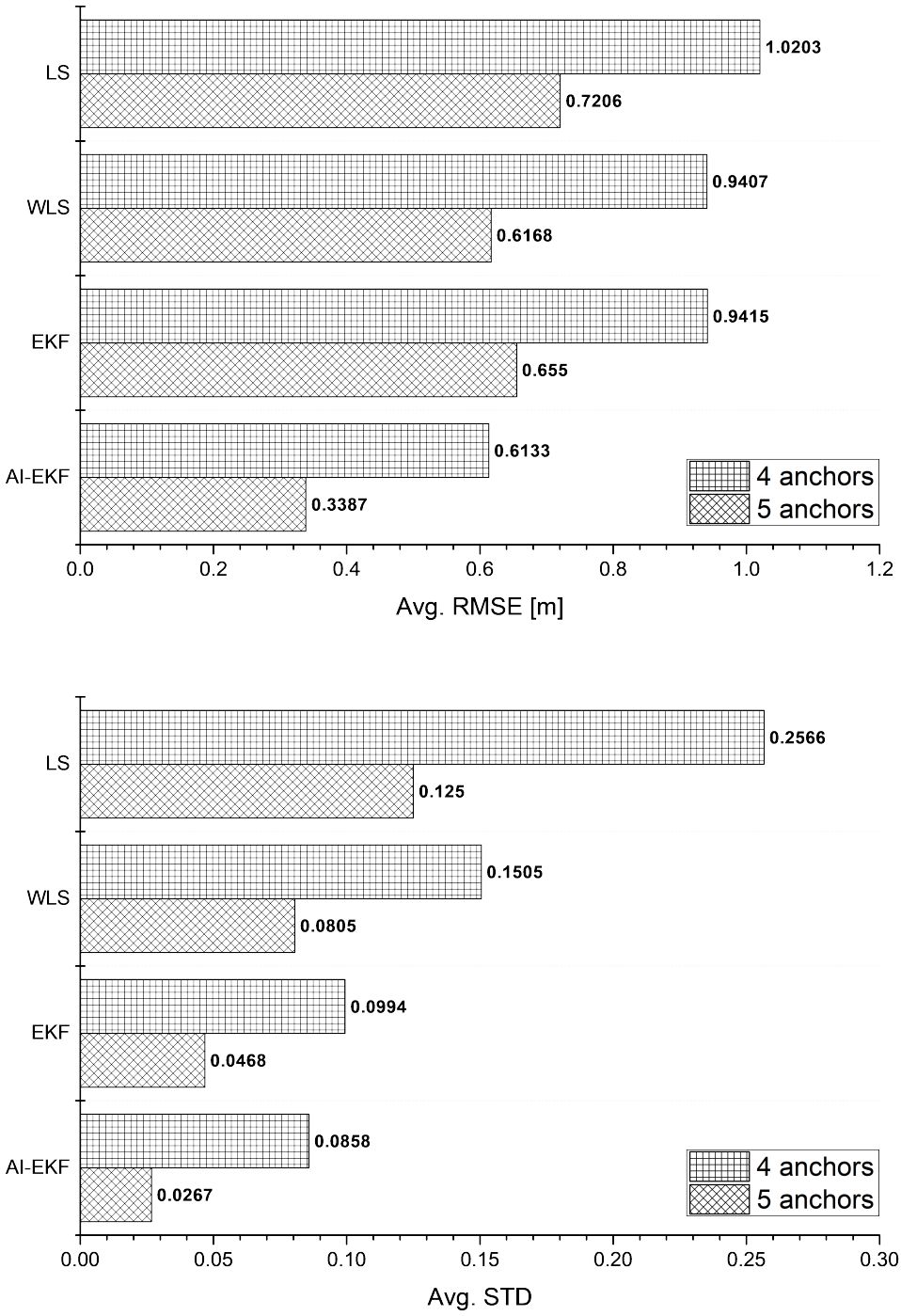

Figure 34. Average RMSE (top) and STD (bottom) for each route of each method for anchor deployments in scenario KNOWN.

3) Scenario UNKNOWN Using Four Anchors

Fig. 35, 36, and 37 present trajectories and CDFs of positioning errors for each method in scenario UNKNOWN using four anchors. Tables 17 and 18 also present the RMSE and STD values for each method. Furthermore, Fig. 41 shows the average RMSE and STD for routes of each method. The deployment of anchors was divided into office groups (A1, A5, and A6) and one corridor (A3), similar to the scenario KNOWN. However, this scenario had different UWB channel conditions from scenario KNOWN. The worst zone was generated around P6 and P9 because of reasons such as concrete pillars, tempered glasses, stainless steel frames, and human bodies. Therefore, WLS and EKF exhibited similar performance improvements as on the 8th floor. WLS achieved an average RMSE of 4.5 % and an average STD of 40 % compared to LS, while EKF improved the average STD of 172.8 % compared to LS. However, it reduced the performance of the average RMSE of -2.7 % because the insufficient number of anchors triggers the majority ratio of NLOS channels. The average RMSE and STD of the AI-EKF were enhanced by 95.6 % and 309.9 % compared to LS. Note that the trained model of AI-EKF did not learn CIRs in this environment. However, it successfully mitigated NLOS effects because the LSTM network optimally classified the channel status, irrespective of the environmental conditions. In other words, the proposed labeling of the channels provides flexibility to the design and can employ the proposed AI model for positioning services.

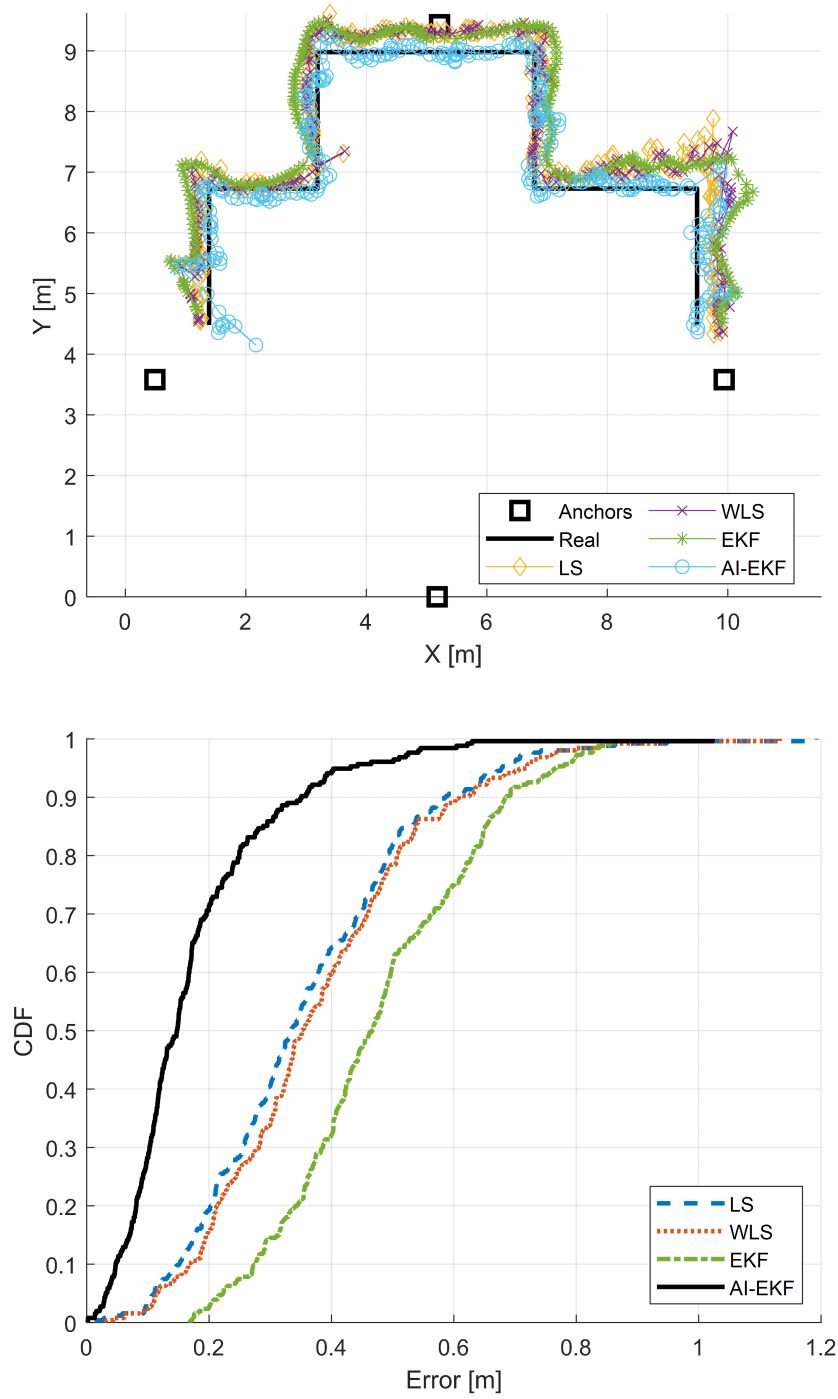

Figure 35. Trajectories (top) and positioning error CDFs (bottom) measured by each method in the office on the 2nd floor using four anchors.

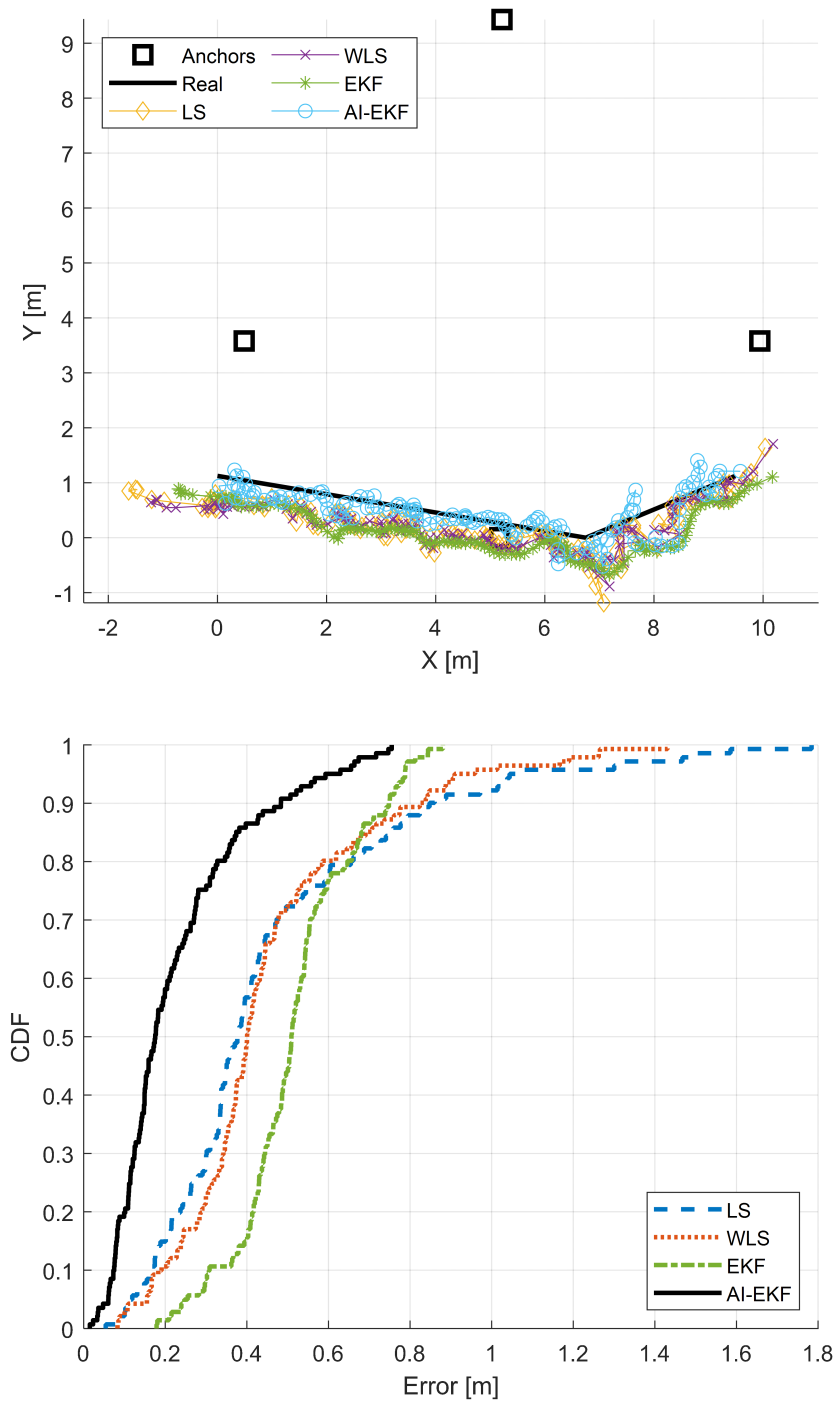

Figure 36. Trajectories (top) and positioning error CDFs (bottom) measured by each method in the corridor on the 2nd floor using four anchors.

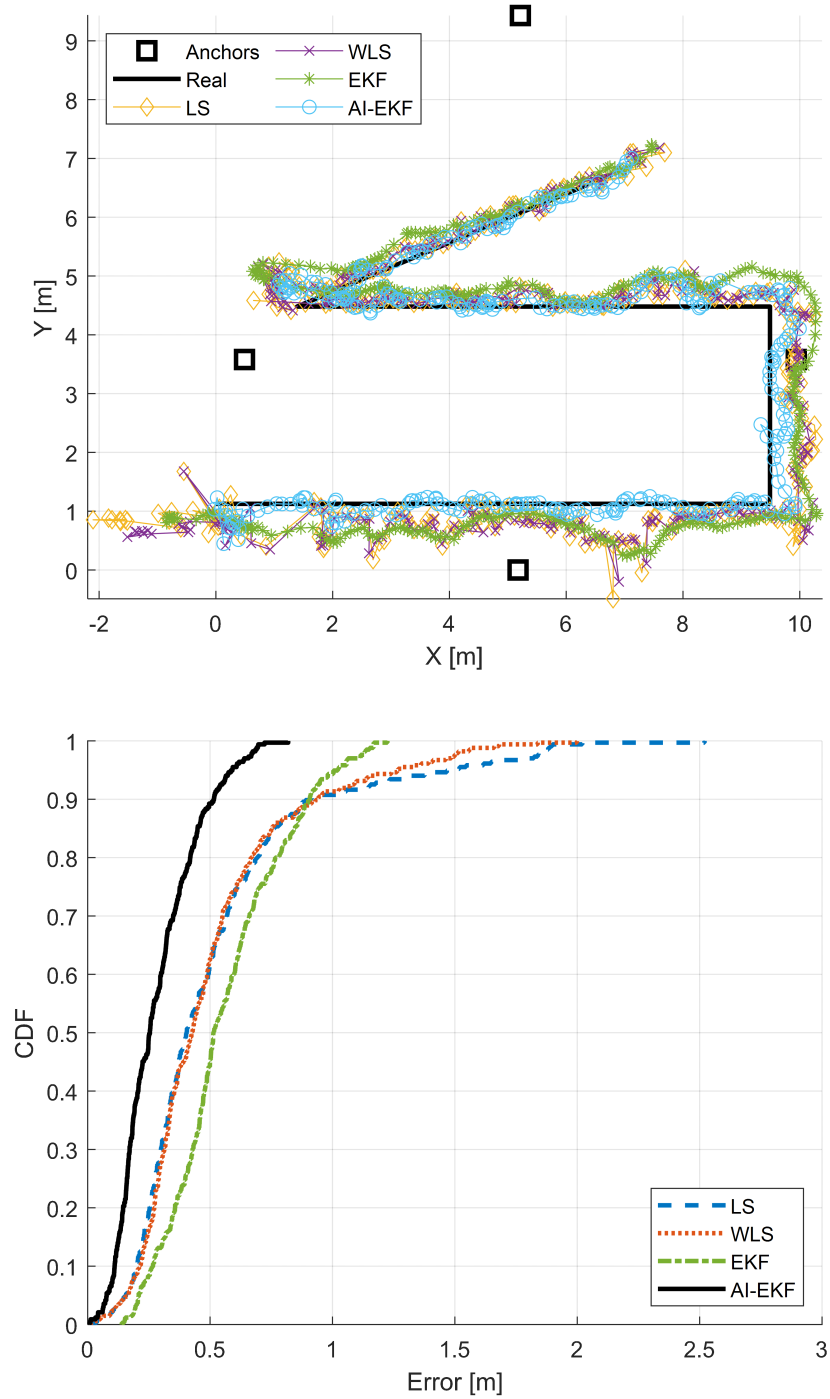

Figure 37. Trajectories (top) and positioning error CDFs (bottom) measured by each method in both the office and corridor on the 2nd floor using four anchors.

Table 17. RMSE of positioning results at each method in scenario UNKNOWN using four anchors.

Methods	Laboratory [m]	Corridor [m]	Both [m]
LS	0.3998	0.5583	0.6519
WLS	0.4159	0.5204	0.604
EKF	0.5042	0.5388	0.6121
AI-EKF	0.2189	0.281	0.323

Table 18. STD of positioning errors at each method in scenario UNKNOWN using four anchors.

Methods	Laboratory	Corridor	Both
LS	0.0317	0.0991	0.1537
WLS	0.0314	0.0623	0.1095
EKF	0.0258	0.0218	0.0567
AI-EKF	0.0173	0.0273	0.0248

4) Scenario UNKNOWN Using Five Anchors

Fig. 38, 39, and 40 present trajectories and CDFs of positioning errors for each method in scenario UNKNOWN. Tables 19 and 20 also present RMSE and STD values for each method. The deployment of anchors was divided into office (A2, A4, and A7) and corridor (A0 and A8) groups, similar to the scenario KNOWN. WLS achieved average RMSE and STD values of 17.6 % and 68.6 % compared to LS, while EKF achieved average RMSE and STD values of 7.4 % and 100.1 % compared to LS. The average RMSE and STD values of AI-EKF were enhanced by 114.7 % and 454.5 %, respectively, compared to LS.

The additional anchor deployed at the corridor enhanced the positioning performance more than that of the case with four anchors. In this scenario, as illustrated Fig. 41, LS maintained its positioning performance of an average RMSE and improved average STD of 35 %. WLS achieved the improvement of an average RMSE of 12.8 % and average STD of 62.6 %. EKF improved an average RMSE of 10.6 % and maintained its average STD similarly. In addition, the average RMSE and STD of AI-EKF were enhanced by 9.9 % and 82.6 %.

The CDFs of the positioning errors in both scenarios also indicate that the AI-EKF in the proposed system exhibited a better positioning performance than the other existing methods. Hence, it can be inferred that the proposed system mitigates the NLOS effects of the UWB system.

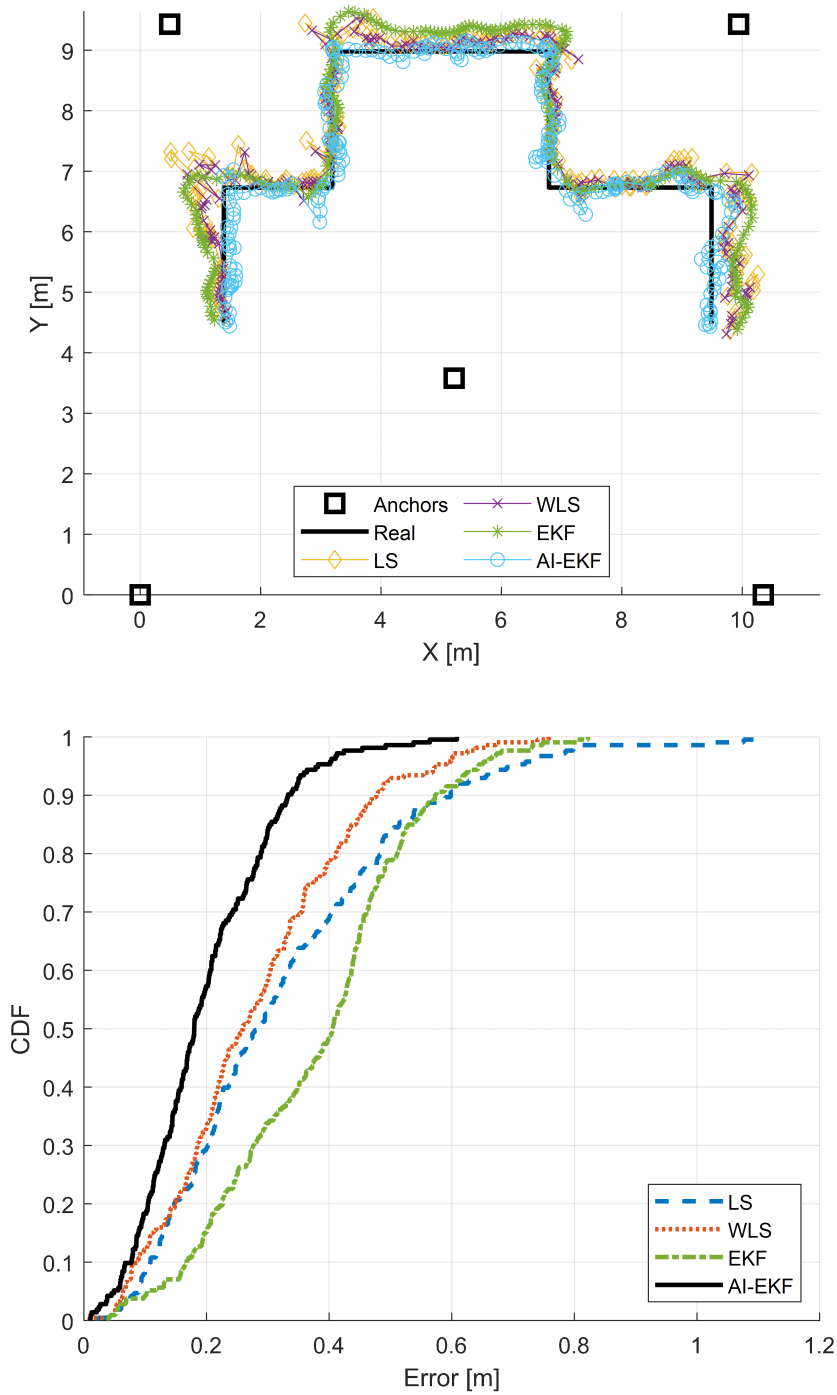

Figure 38. Trajectories (top) and positioning error CDFs (bottom) measured by each method in the office on the 2nd floor using five anchors.

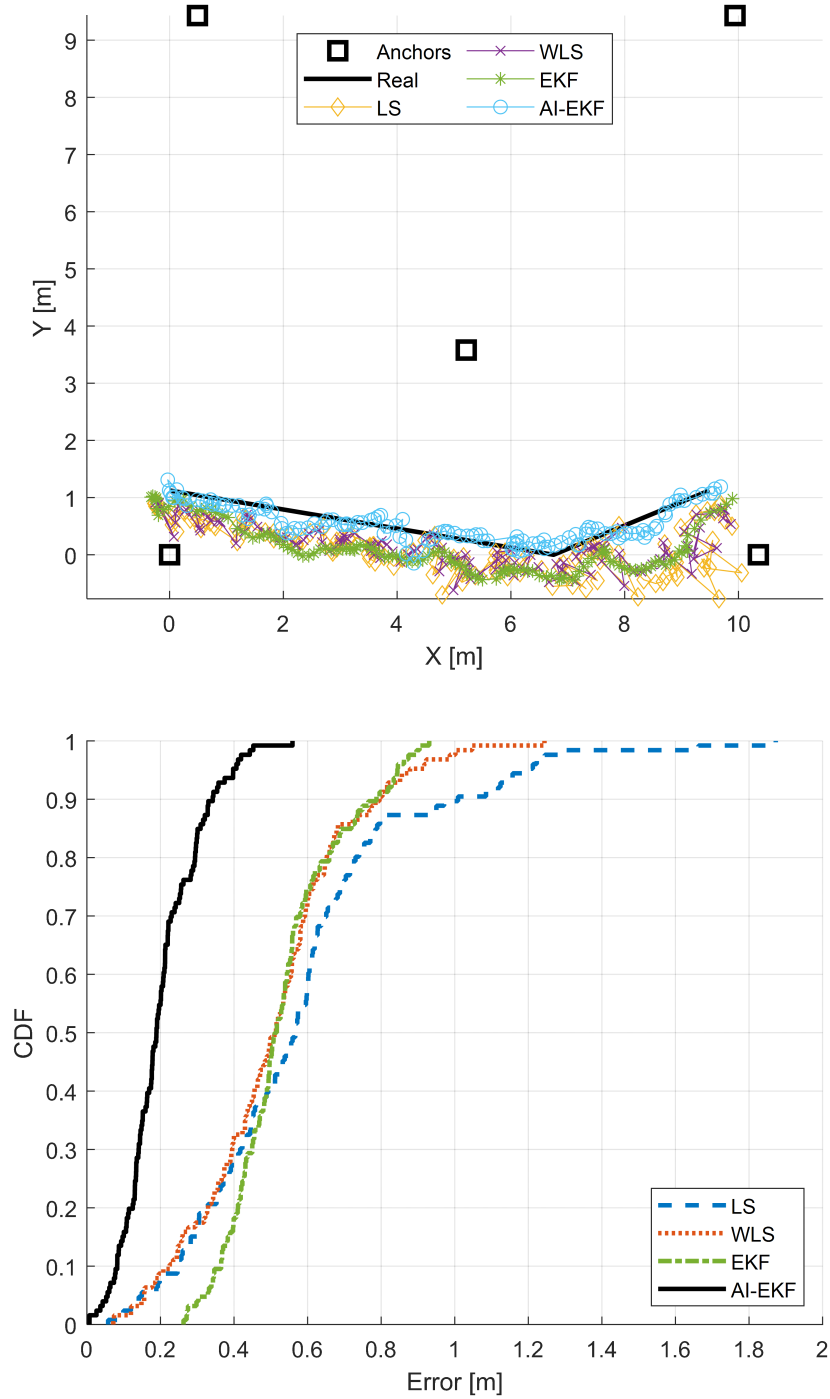

Figure 39. Trajectories (top) and positioning error CDFs (bottom) measured by each method in the corridor on the 2nd floor using five anchors.

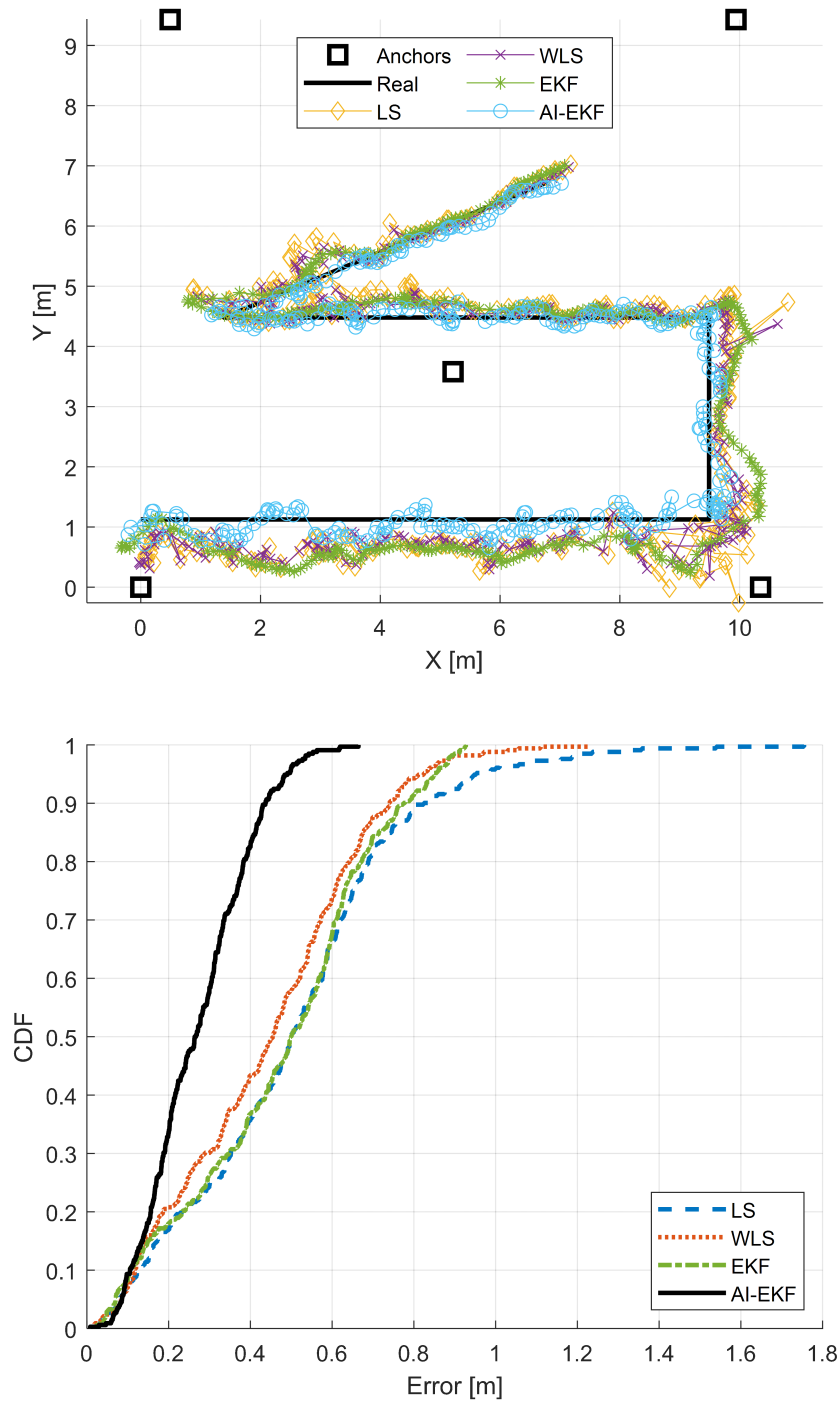

Figure 40. Trajectories (top) and positioning error CDFs (bottom) measured by each method in both the office and corridor on the 2nd floor using five anchors.

Table 19. RMSE of positioning results at each method in scenario UNKNOWN using five anchors.

Methods	Laboratory [m]	Corridor [m]	Both [m]
LS	0.3799	0.6551	0.5718
WLS	0.3184	0.5489	0.4986
EKF	0.4122	0.5565	0.528
AI-EKF	0.2239	0.2254	0.2992

Table 20. STD of positioning errors at each method in scenario UNKNOWN using five anchors.

Methods	Laboratory	Corridor	Both
LS	0.0392	0.0942	0.0773
WLS	0.0231	0.0464	0.0555
EKF	0.026	0.0234	0.0559
AI-EKF	0.0115	0.0105	0.016

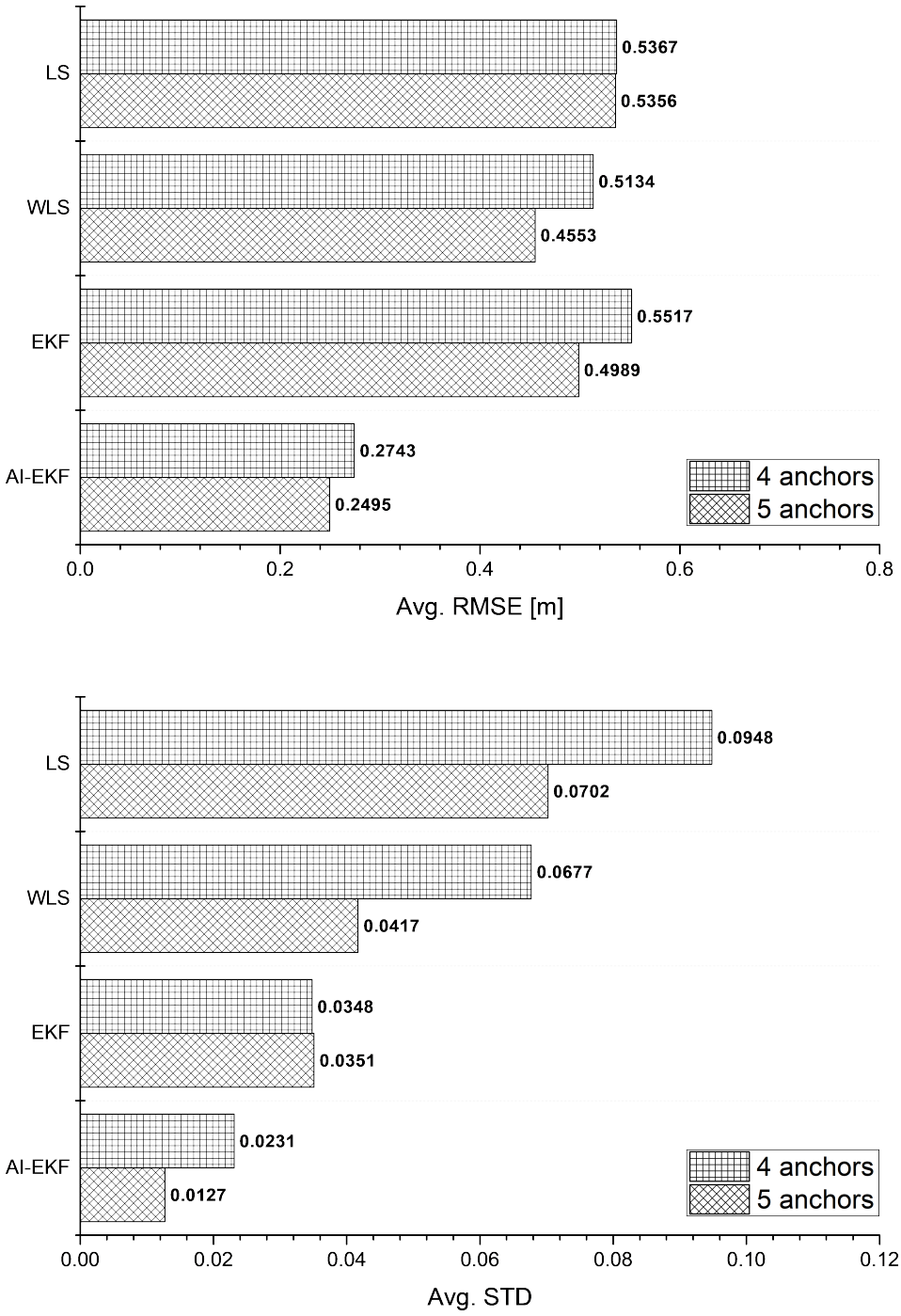

Figure 41. Average RMSE (top) and STD (bottom) for each route of each method for anchor deployments in scenario UNKNOWN.

VI. Conclusion

This thesis proposed the AI-applied UWB positioning system with an AI-EKF localization based on LSTM and EKF localization. In the proposed method, the system determines the channel conditions for NLOS error mitigation. Then, the statistics of the channel are used to mitigate the NLOS effects from the TWR measurement. Finally, the user obtains an enhanced position using EKF localization with an NLOS-mitigated measurement. The proposed method was compared with existing localization methods in two experimental scenarios. In both scenarios, the proposed method mitigated the NLOS-biased error and enhanced the positioning accuracy. Moreover, it exhibited a superior positioning precision owing to the attached EKF algorithm. Additionally, even in scenario UNKNOWN using five anchors, the proposed AI-EKF method showed an average improvement of RMSE of 82.5 % and 100 % in terms of positioning error compared to existing methods WLS and EKF, respectively. Furthermore, it exhibited improved precision on trajectories with an average STD of 228.9 % and 177.1 % compared to WLS and EKF, respectively. In conclusion, the proposed UWB positioning system using UWB channel classification with LSTM network and NLOS effect mitigation with EKF can provide more accurate positioning solutions as compared to existing methods even in the case of no training on the channel conditions at the current tag position.

References

[1] J. Kunhoth, A. Karkar, S. Al-Maadeed, and A. Al-Ali, “Indoor positioning and wayfinding systems: a survey,” *Human-centric Computing and Information Sciences*, vol. 10, no. 18, pp. 1-41, May 2020.

[2] O. Danielsson, M. Holm, and A. Syberfeldt, “Augmented reality smart glasses in industrial assembly: Current status and future challenges,” *Journal of Industrial Information Integration*, vol. 20, Dec. 2020, Art. no. 100175.

[3] W. Giernacki, M. Skwierczyński, W. Witwicki, P. Wroński, and P. Kozierski, “Crazyflie 2.0 quadrotor as a platform for research and education in robotics and control engineering,” in *International Conference on Methods and Models in Automation and Robotics (MMAR)*, Miedzyzdroje, Poland, 2017, pp. 37-42.

[4] A. Umek and A. Kos, “Validation of UWB positioning systems for player tracking in tennis,” *Personal and Ubiquitous Computing*, pp. 1-11, Nov. 2020.

[5] L. Zamora-Cadenas, I. Velez, and J. E. Sierra-Garcia, “UWB-Based Safety System for Autonomous Guided Vehicles Without Hardware on the Infrastructure,” *IEEE Access*, vol. 9, pp. 96430-96443, Jul. 2021.

[6] L. Barbieri, M. Brambilla, A. Trabattoni, S. Mervic, and M. Nicoli, “UWB Localization in a Smart Factory: Augmentation Methods and Experimental Assessment,” *IEEE Transactions on Instrumentation and Measurement*, vol. 70, no. 2508218, pp. 1-18, Apr. 2021.

[7] IEEE Standard for Local and metropolitan area networks--Part 15.4: Low-Rate Wireless Personal Area Networks (LR-WPANs), IEEE Standard 802.15.4-2011 (Revision of IEEE Std 802.15.4-2006), 2011.

[8] IEEE Standard for Wireless Medium Access Control (MAC) and Physical Layer (PHY) Specifications for Peer Aware Communications (PAC), IEEE Standard 802.15.8-2017, 2018.

[9] J. R. Fernandes and D. Wentzloff, “Recent advances in IR-UWB transceivers: An overview,” in *Proceedings of 2010 IEEE International Symposium on Circuits and Systems*, Paris, France, 2010, pp. 3284-3287.

[10] C. M. De Dominicis et al., “High-precision UWB-based timestamping,” in *IEEE International Symposium on Precision Clock Synchronization for Measurement, Control and Communication*, Munich, Germany, 2011, pp. 50-55.

[11] P. Carbone et al., “Low Complexity UWB Radios for Precise Wireless Sensor Network Synchronization,” *IEEE Transactions on Instrumentation and Measurement*, vol. 62, no. 9, pp. 2538-2548, Sep. 2013.

[12] Z. Sahinoglu, S. Gezici, and I. Guvenc, “Ultra-Wideband Positioning Systems: Theoretical Limits Ranging Algorithms and Protocols,” in *Cambridge Univ. Press*, U.K.:Cambridge, 2008, pp. 70-73.

[13] J. Tiemann, Y. Elmasry, L. Koring, and C. Wietfeld, “ATLAS FaST: Fast and Simple Scheduled TDOA for Reliable Ultra-Wideband Localization,” in *International Conference on Robotics and Automation (ICRA)*, Montreal, QC, Canada, 2019, pp. 2554-2560.

[14] C. Lian Sang, M. Adams, T. Hörmann, M. Hesse, M. Porrmann, and U. Rückert, “Numerical and Experimental Evaluation of Error Estimation for Two-Way Ranging Methods,” *Sensors*, vol. 19, no. 3, Feb. 2019, Art. no. 616.

[15] I. Guvenc and C. Chong, “A Survey on TOA Based Wireless Localization and NLOS Mitigation Techniques,” *IEEE Communications Surveys & Tutorials*, vol. 11, no. 3, pp. 107-124, Aug. 2009.

[16] Y. Jiang and V. C. M. Leung, “An Asymmetric Double Sided Two-Way Ranging for Crystal Offset,” in *International Symposium on Signals, Systems and Electronics*, Montreal, QC, Canada, 2007, pp. 525-528.

[17] I. Domuta and T. P. Palade, “Two-Way Ranging Algorithms for Clock Error Compensation,” *IEEE Transactions on Vehicular Technology*, vol. 70, no. 8, pp. 8237-8250, Aug. 2021.

[18] O. S. Oguejiofor, A. N. Aniedu, H. C. Ejiofor, and A. U. Okolibe, “Trilateration based localization algorithm for wireless sensor network”, *International Journal of Science and Modern Engineering*, vol. 1, no. 10, pp. 21-27, Sep. 2013.

[19] E. Theussl, D. Ninevski, and P. O'Leary, "Measurement of Relative Position and Orientation using UWB," in *IEEE International Instrumentation and Measurement Technology Conference (I2MTC)*, Auckland, New Zealand, 2019, pp. 1-6.

[20] D. Feng, C. Wang, C. He, Y. Zhuang, and X. Xia, "Kalman-Filter-Based Integration of IMU and UWB for High-Accuracy Indoor Positioning and Navigation," *IEEE Internet of Things Journal*, vol. 7, no. 4, pp. 3133-3146, Apr. 2020.

[21] K. Bregar and M. Mohorčič, "Improving Indoor Localization Using Convolutional Neural Networks on Computationally Restricted Devices," *IEEE Access*, vol. 6, pp. 17429-17441, Mar. 2018.

[22] G. Welch and G. Bishop, "An introduction to the Kalman filter," Dept. Comput. Sci., Univ. North Carolina Chapel Hill, Chapel Hill, NC, USA, Tech. Rep. TR 95-041, Jul. 2006.

[23] J. T. Jang, A. Santamaria-Navarro, B. T. Lopez, and A. -a. Agha-mohammadi, "Analysis of State Estimation Drift on a MAV Using PX4 Autopilot and MEMS IMU During Dead-reckoning," in *IEEE Aerospace Conference*, Big Sky, MT, USA, 2020, pp. 1-11.

[24] A. R. Jiménez, F. Seco, J. C. Prieto, and J. Guevara, "Indoor pedestrian navigation using an INS/EKF framework for yaw drift reduction and a foot-mounted IMU," in *Workshop on Positioning, Navigation and Communication*, Dresden, Germany, 2010, pp. 135-143.

[25] R. Toledo-Moreo, M. A. Zamora-Izquierdo, B. Ubeda-Minarro, and A. F. Gomez-Skarmeta, "High-Integrity IMM-EKF-Based Road Vehicle Navigation With Low-Cost GPS/SBAS/INS," *IEEE Transactions on Intelligent Transportation Systems*, vol. 8, no. 3, pp. 491-511, Sep. 2007.

[26] T. Kim and T. H. Park, "Extended Kalman Filter (EKF) Design for Vehicle Position Tracking Using Reliability Function of Radar and Lidar," *Sensors*, vol. 20, no. 15, Jul. 2020, Art. no. 4126.

[27] A. Albaidhani, A. Morell, and J. L. Vicario, “Ranging in UWB using commercial radio modules: Experimental validation and NLOS mitigation,” in *Indoor Positioning and Indoor Navigation (IPIN)*, Alcala de Henares, Spain, 2016, pp. 1-7.

[28] D.-H. Kim, G.-R. Kwon, J.-W. Kim, and J.-Y. Pyun, “NLOS identification in UWB channel for indoor positioning," in *IEEE Annual Consumer Communications & Networking Conference (CCNC)*, Las Vegas, NV, USA, 2018, pp. 1-4.

[29] S. Guo, Y. Zhang, X. Gui, and L. Han, “An Improved PDR/UWB Integrated System for Indoor Navigation Applications,” *IEEE Sensors Journal*, vol. 20, no. 14, pp. 8046-8061, 15 Jul. 2020.

[30] D.-H. Kim and J.-Y. Pyun, “NLOS Identification Based UWB and PDR Hybrid Positioning System,” *IEEE Access*, vol. 9, pp. 102917-102929, Jul. 2021.

[31] V. F. Miramá, L. E. Díez, A. Bahillo, and V. Quintero, “A Survey of Machine Learning in Pedestrian Localization Systems: Applications, Open Issues and Challenges,” *IEEE Access*, vol. 9, pp. 120138-120157, Aug. 2021.

[32] T. Wang, K. Hu, Z. Li, K. Lin, J. Wang, and Y. Shen, “A Semi-Supervised Learning Approach for UWB Ranging Error Mitigation,” *IEEE Wireless Communications Letters*, vol. 10, no. 3, pp. 688-691, Mar. 2021.

[33] A. G. Ferreira, D. Fernandes, S. Branco, A. P. Catarino, and J. L. Monteiro, “Feature Selection for Real-Time NLOS Identification and Mitigation for Body-Mounted UWB Transceivers,” *IEEE Transactions on Instrumentation and Measurement*, vol. 70, no. 5502310, pp. 1-10, Apr. 2021.

[34] A. Musa, G. D. Nugraha, H. Han, D. Choi, S. Seo, and J. Kim, “A decision tree-based NLOS detection method for the UWB indoor location tracking accuracy improvement,” *International Journal of Communication Systems*, vol. 32, no. 13, Jun. 2019, Art. no. e3997.

[35] C. L. Sang, B. Steinhagen, J. D. Homburg, M. Adams, M. Hesse, and U.

Rückert, “Identification of NLOS and multi-path conditions in UWB localization using machine learning methods,” *Applied Sciences*, vol. 10, no. 11, pp. 1-25, Jan. 2020.

[36] J. Fan and A. S. Awan, “Non-Line-of-Sight Identification Based on Unsupervised Machine Learning in Ultra Wideband Systems,” *IEEE Access*, vol. 7, pp. 32464-32471, Mar. 2019.

[37] K. Bregar et al., “NLOS channel detection with multilayer perceptron in low-rate personal area networks for indoor localization accuracy improvement,” in *Proc. 8th Jožef Stefan Int. Postgraduate School Students Conf.*, Ljubljana, Slovenia, 2016, pp. 1-8.

[38] C. Jiang, S. Chen, Y. Chen, D. Liu, and Y. Bo, “An UWB Channel Impulse Response De-Noising Method for NLOS/LOS Classification Boosting,” *IEEE Communications Letters*, vol. 24, no. 11, pp. 2513-2517, Nov. 2020.

[39] Z. Cui, T. Liu, S. Tian, R. Xu, and J. Cheng, “Non-Line-of-Sight Identification for UWB Positioning Using Capsule Networks,” *IEEE Communications Letters*, vol. 24, no. 10, pp. 2187-2190, Oct. 2020.

[40] C. Jiang, J. Shen, S. Chen, Y. Chen, D. Liu, and Y. Bo, “UWB NLOS/LOS Classification Using Deep Learning Method,” *IEEE Communications Letters*, vol. 24, no. 10, pp. 2226-2230, Oct. 2020.

[41] M. Stahlke, S. Kram, C. Mutschler and T. Mahr, “NLOS Detection using UWB Channel Impulse Responses and Convolutional Neural Networks,” in *International Conference on Localization and GNSS (ICL-GNSS)*, Tampere, Finland, 2020, pp. 1-6.

[42] Decawave Ltd., APS006 Part 2 Application Note: Non Line of Sight Operation and Optimizations to improve Performance in DW1000 Based Systems 1.5, 2017. [Online]. Available: https://www.decawave.com, accessed on: Oct. 2021

[43] B. Alavi and K. Pahlavan, “Modeling of the TOA-based distance measurement error using UWB indoor radio measurements,” *IEEE Communications Letters*,

vol. 10, no. 4, pp. 275-277, Apr. 2006.

[44] J. Khodjaev, Y. Park, and A. Saeed Malik, “Survey of NLOS identification and error mitigation problems in UWB-based positioning algorithms for dense environments,” *Annals of Telecommunications*, vol. 65, no. 5, pp. 301-311, Aug. 2009.

[45] Y. Wang, K. Gu, Y. Wu, W. Dai, and Y. Shen, “NLOS Effect Mitigation via Spatial Geometry Exploitation in Cooperative Localization,” *IEEE Transactions on Wireless Communications*, vol. 19, no. 9, pp. 6037-6049, Sep. 2020.

[46] X. Yang, “NLOS Mitigation for UWB Localization Based on Sparse Pseudo-Input Gaussian Process,” *IEEE Sensors Journal*, vol. 18, no. 10, pp. 4311-4316, May 2018.

[47] X. Yang, J. Wang, D. Song, B. Feng, and H. Ye, “A Novel NLOS Error Compensation Method Based IMU for UWB Indoor Positioning System,” *IEEE Sensors Journal*, vol. 21, no. 9, pp. 11203-11212, May 2021.

[48] G. Bellusci, G. J. M. Janssen, J. Yan, and C. C. J. M. Tiberius, “Model of distance and bandwidth dependency of TOA-based UWB ranging error,” in *IEEE International Conference on Ultra-Wideband*, Hannover, Germany, 2008, pp. 193-196.

[49] A. R. Jiménez Ruiz, and F. Seco Granja, “Comparing Ubisense, BeSpoon, and DecaWave UWB Location Systems: Indoor Performance Analysis,” *IEEE Transactions on Instrumentation and Measurement*, vol. 66, no. 8, pp. 2106-2117, Aug. 2017.

[50] Decawave Ltd., DW1000 User Manual: How to Use, Configure and Program The DW1000 UWB Transceiver 2.16, 2017. [Online]. Available: https://www.decawave.com, accessed on: Oct. 2021

[51] 장지수, “딥러닝에 목마른 사람들을 위한 Pytorch,” 비제이퍼블릭, Jun. 2019.

[52] Francois Chollet, “케라스 창시자에게 배우는 딥러닝: Deep Learning with Python by Francois Chollet,” 길벗, Oct. 2018.

[53] 사이토 고키, “밑바닥부터 시작하는 딥러닝: 파이썬으로 익히는 딥러닝 이론과 구현,” 한빛미디어, Jan. 2017.

[54] S. Hochreiter and J. Schmidhuber, “Long short-term memory,” *Neural Computation*, vol. 9, no. 8, pp. 1735-1780, Nov. 1997.

[55] Y. Bengio, P. Simard, and P. Frasconi, “Learning long-term dependencies with gradient descent is difficult,” *IEEE Transactions on Neural Networks*, vol. 5, no. 2, pp. 157-166, Mar. 1994.

[56] Decawave Ltd., APS016 Application Note: A discussion of the elements to consider when developing a commercial product based on the TREK1000 Two-Way-Ranging (TWR) RTLS IC Evaluation Kit 2.3, 2018. [Online]. Available: https://www.decawave.com, accessed on: Oct. 2021

[57] F. Despaux, K. Jaffrès-Runser, A. van den Bossche, and T. Val, “Accurate and platform-agnostic time-of-flight estimation in ultra-wide band,” in *IEEE Annual International Symposium on Personal, Indoor, and Mobile Radio Communications (PIMRC)*, Valencia, Spain, 2016, pp. 1-7.

[58] H. Kim, “Double-sided two-way ranging algorithm to reduce ranging time,” *IEEE Communications Letters*, vol. 13, no. 7, pp. 486-488, Jul. 2009.

[59] Decawave Ltd., DW1000 Device Driver Application Programming Interface (API) Guide: Using API Functions to Configure and Program The DW1000 UWB Transceiver 2.7, 2017. [Online]. Available: https://www.decawave.com, accessed on: Oct. 2021

[60] P. Koopman, “32-bit cyclic redundancy codes for Internet applications,” in *Proceedings International Conference on Dependable Systems and Networks*, Pittsburgh, PA, USA, 2002, pp. 459-468.

[61] Decawave Ltd., APS013 Application Note: The implementation of two-way ranging with the DW1000 2.2, 2017. [Online]. Available: https://www.decawave.com, accessed on: Oct. 2021

[62] ARM MBED, Mbed OS 6.10. [Online]. Available: https://github.com/ARMmbed/mbed-os, accessed on: Apr. 2021

[63] A. Graves and J. Schmidhuber, “Framewise phoneme classification with bidirectional LSTM and other neural network architectures,” *Neural Networks*, vol. 18, no. 5, pp. 602-610, Jul. 2005.

[64] J. Chung, C. Gulcehre, K. Cho and Y. Bengio, Empirical evaluation of gated recurrent neural networks on sequence modeling, Dec. 2014, [online]. Available: http://arxiv.org/abs/1412.3555, accessed on: Oct. 2021

[65] Srivastava, N., G. Hinton, A. Krizhevsky, I. Sutskever, and R. Salakhutdinov, “Dropout: A Simple Way to Prevent Neural Networks from Overfitting,” *Journal of Machine Learning Research*, vol. 15, pp. 1929-1958, Jun. 2014.

[66] Krizhevsky, A., I. Sutskever, and G. E. Hinton, “ImageNet Classification with Deep Convolutional Neural Networks,” *Advances in Neural Information Processing Systems*, vol. 25, pp. 1097-1105, May 2012.

[67] M. H. Beale, M. T. Hagan, and H. B. Demuth, Deep Learning Toolbox™ User's Guide 2021a, 2021. [Online]. Available: https://www.mathworks.com/products/matlab.html, accessed on: Oct. 2021

[68] M. Kolakowski and J. Modelski, “First path component power based NLOS mitigation in UWB positioning system,” in *Telecommunication Forum (TELFOR)*, Belgrade, Serbia, 2017, pp. 1-4.

[69] Y. Huang, Y. Zhang, B. Xu, Z. Wu, and J. A. Chambers, “A New Adaptive Extended Kalman Filter for Cooperative Localization,” *IEEE Transactions on Aerospace and Electronic Systems*, vol. 54, no. 1, pp. 353-368, Feb. 2018.

[70] T. Otim, A. Bahillo, L. E. Díez, P. Lopez-Iturri, and F. Falcone, “Impact of Body Wearable Sensor Positions on UWB Ranging,” *IEEE Sensors Journal*, vol. 19, no. 23, pp. 11449-11457, Dec. 2019.

[71] H. Ferdowsi, S. Jagannathan, and M. Zawodniok, “An Online Outlier Identification and Removal Scheme for Improving Fault Detection Performance,” *IEEE Transactions on Neural Networks and Learning Systems*, vol. 25, no. 5, pp. 908-919, May 2014.